The use of microbial rhodopsin proteins in differential photodetection

Louisa Reissig[1,2]*, Kirstin Buchanan[2,3], Thea Lindner[1], Marie Kurihara[4], Po-Chuan Chan[1], Falk Kibowski[1], Keiichi Kojima[4], Simon Dalgleish[2], Kunio Awaga[2] and Yuki Sudo[4]

[1]Institute of Experimental Physics, Freie Universitat Berlin, Arnimallee, Berlin, Germany, [2]Department of Chemistry and Research Centre for Material Sciences, Nagoya Univeristy, Furo-cho, Nagoya, Japan, [3]School of Chemistry, University of Edinburgh, Edinburgh, United Kingdom, [4]Graduate School of Medicine, Dentistry and Pharmaceutical Sciences, Okayama University, Okayama, Japan

Transferring information using light signals, and detecting these signals, is not only a cornerstone of modern technology, but has been essential for organisms since evolution provided them with proteins - the cell's custom-built tools - capable of light to energy conversion or photo-sensing. In this study, the use of diverse representatives of the photoactive protein family of microbial rhodopsins as the active material in differential photodetector devices has been investigated. By modifying the internal parameters of the detectors, such as rhodopsin kind, salinity and pH, as well as by tuning the external environment, such as temperature, we could increase the responsivity and speed of our devices by over 2 orders of magnitude, compared to a previously reported proof-of-concept device, to the µA/W and kHz range, respectively. The characteristic differential photodetector transient signal shape could be stably observed for temperatures up to 70°C and related to features in the protein's cyclic reaction upon light activation, with the changes in photocurrent shape and polarity concomitantly providing information about the protein used in the device. Furthermore, this study demonstrates that the use of proteins - the cell's molecular machines - instead of simple organic semiconductor materials can add secondary sensor functionalities to the device if the stimulus (here through temperature and pH) has sufficient effect on the photocurrent signal to allow calibration.

KEYWORDS

photodetection, microbial rhodopsin, MISM photodetector, biotechnology, impedance spectroscopy

1 Introduction

Converting light to electric energy has become increasingly important in recent decades. It was early recognized that sunlight is our ultimate energy source, which can induce a variety of chemical, as well as electron-transfer, reactions used in natural and artificial systems for information processing and the generation of energy [1]. While sunlight has provided us through the geological eras with fossil fuels, a non-renewable energy source by human timescales, which we are eagerly consuming day by day, it was soon recognised that we were not taking full advantage of the extraordinary amount of energy provided to us every day by the sun [1, 2]. Despite the early discovery of the photoelectrical effect in 1839 [3, 4], it was only in 1954 that the first inorganic solar cells were introduced [3, 5]. Today

Si-based solar cells dominate the market, with demands growing exponentially and with the global solar capacity having crossed the TW (10^{12}) line in 2022 [6], driven by an increasing move towards renewable energy sources to fuel our energy demands. Moreover, light-to-electric energy conversion plays a decisive role in today's information technology [7], since it was recognised that information can quickly, reliably and easily be transferred through optical signals, as well as through the move towards digital photography and filming, readily facilitating advanced digital image processing. In all cases, increasing research has been devoted to developing more efficient and/or more optimised devices for the given application [8–12]. With increasing demands, attention has also been directed towards the type and footprint of materials used in such opto-electronic devices, as full life cycles are increasingly considered, not only considering the used materials and energy consumption in their production (such as purification of materials), but also the recycling costs and materials re-usability of the devices [13–15]. This has driven the search for so-called "green" materials, such as organic materials, either synthetic or derived from natural resources, and with it the move towards organic devices, with the first organic solar cells being reported in 1986 [16], with efficiencies above 19% published recently for more optimised device architectures [17]. Besides promising cheap, flexible and green consumer electronics, a major benefit of organic opto-electronic materials is that their structure can be easily tuned to absorb or emit light at a desired wavelength range. Nevertheless, the only successful organic opto-electronic devices, that have made the transition to mass-market by today, relies on the opposite conversion, i.e., that of electric energy to light, in the form of organic LEDs [18].

While small organic molecules, such as glucose or adenosine triphosphate (ATP), are important for living organisms, either as fuel or by providing biosynthetic energy through donating its terminal phosphate groups to other molecules, the biochemistry of life is largely facilitated by the interplay of macromolecules, such as proteins (the cell's molecular machines), whose blueprints are stored in the genetic code of the DNA [19, 20]. Most of life revolves around the activities of proteins - the energy of the cell goes largely into making them, and then into using them to perform a multitude of diverse jobs. Each protein has its own amino-acid sequence. The poly-peptide chain is folded into a 3D structure, featuring certain secondary structural elements, such as alpha-helices and beta-strands, stabilised by a range of hydrogen bonds and cysteine bridges. Often in combination with metals or small organic molecules, or after combining with other proteins to higher order complexes, they perform specific functions in the cell. Proteins are not only sensitive to point-mutations of certain structurally decisive amino-acids, but also to factors which affect the weak bonding that holds them together, especially to changes in pH and temperature, which can rapidly denature them or deactivate their functionalities through conformational changes or (de-)protonation of specific amino-acids [19–21]. Despite the vast number of different proteins, they can be classified into protein families based on similarities in secondary structural elements and functionality. Proteins facilitate biochemical reactions, as enzymes, by lowering their activation energy, and are, in contrast to non-biological catalysts, highly selective, and thus not considered general-purpose but rather custom-built tools, with the cell requiring a different enzyme for practically every reaction it carries out [19–21]. As a result, the cell has the ability to influence its metabolic pathway, by controlling the type and amounts of proteins present [19–21]. Enzymes can now be also found as regular tools used in industrial synthetic chemistry [22].

Through the use of proteins, light to energy conversion can be achieved in living cells, with photoinduced electron transfer being the underlying principle of photosynthesis [19, 21], used to prepare the various high-energy molecules (such as glucose or starch). Those molecules can be broken down to release the necessary energy to drive the various endergonic bio-reactions. Moreover, photosynthesis is also crucial for our climate, removing CO_2 from our atmosphere and supplying us with O_2. Those high-energy molecules provide the necessary fuel to animals, which have no primary energy source, but can break down those molecules with the help of O_2 in a series of reactions, each time releasing a small amount of energy [19, 21]. In contrast to animals, also non-photosynthetic microbes can use the energy of light as primary energy source through different types of photoactive proteins, such as microbial rhodopsins, the target protein family in this study, which can provide the necessary energy for the synthesis of ATP (considered the unit of energy in a cell) by generating a high proton gradient across the cell membrane (with a reported 10^4fold difference in proton concentration) [1]. The structure of microbial rhodopsins feature seven trans-membrane alpha-helices, linked by short loops on either side of the cell membrane [1, 23]. Covalently attached to a conserved lysine residue in helix G (the sixth helix) as a protonated Schiff base (SB) is its chromophore retinal, which changes its structure from all-trans to 13-cis on excitation with light. The binding of retinal to the protein moiety does not only increase its chemical stability and quantum yield, but also induces a spectral red-shift from its 360 nm absorption maximum in solution, lying in the UV-blue region on the edge of the visible light spectrum, to wavelengths covering a broad range of the visible spectral region (400–600 nm) [24], depending on the specific amino acids and presence of water molecules in the retinal binding pocket and, thus, its local electrostatic environment. The light-induced isomerization of the retinal chromophore leads to sequential conformational changes in the protein moiety, with the consecutive steps summarized in a characteristic photocycle, which takes tenths to several hundreds of ms to complete, and can involve proton or ion transfer steps with the surrounding medium [23, 24].

Besides energy production, photoactive proteins (such as rhodopsins) have been shown to be involved in a variety of functions, like photo-sensing, photo-induced gene expression or the control of e.g., ion channels upon light illumination [21, 25]. In all cases, light-absorption by a chromophore induces structural changes to trigger subsequent reaction cascades. In the process of our vision, we encounter a structural analogue to the microbial rhodopsin, also binding the chromophore retinal (in its 11-cis form). However, here the covalent link to retinal is broken during the photocycle, and all-trans retinal is released to the cytoplasm, requiring the enzyme retinal isomerase for reisomerization to the 11-cis form before reintegration into the opsin [26]. The electrochemical signal induced by the photocycle gets amplified and transferred to the visual nerve, and transmitted via electric

impulses towards the brain (analogous to the signal transfer through the other sensing apparatuses in our body). Interestingly, along with signal amplification and proceeding conversion to electrical impulses, pre-processing steps are often found, used to enhance important signal features (*e.g.*, edge detection). This increases the information processing speed and reduces energetic cost in the brain [27].

In recent years we developed an image sensor design (the DiffEye image sensor), which incorporates the idea of pre-processing of visual information [28]. Here, all pixels are interconnected through a shared liquid dielectric, a decisive component of each photocell. Each photodetector (PD) is based on the so-called MISM (Metal Insulator Semiconductor Metal) design, developed for organic photodetection [29–31], in which the insertion of a thick insulating layer between the photoactive S layer and one of the metal electrodes converts the otherwise DC photocurrent signal into a differential response, with two transient peaks of opposing polarity corresponding to the light-ON and light-OFF process, respectively. The transient signal reflects the charging of the capacitive layer, and the rise and decay times of the signals reflect an interplay of the various RC time constants in the MISM device [32]. Using a liquid dielectric instead of a solid insulating layer in the MISM design allows larger spacing between the M and SM electrodes, as any potential drop is primarily contained within the electric double layers (EDL) forming at the interfaces [30], facilitating deviations from the stacked design to a variety of other architectures [33, 34]. It is also the basis for the interconnection of the photocells in the DiffEye image sensor [28]. Any common electrolyte solution (thus, any biological buffer) can serve as liquid dielectric facilitating the use of photoactive biomolecules as active layers in their native hydrated state. In 2015, we successfully implemented a microbial rhodopsin based active layer in a MISM device [34], adding to the increasing number of optical and optoelectronic artificial devices based on biomolecules, reported in the case of microbial rhodopsins since the 1980s [35–37], with its first proposed use as a holographic medium [38, 39], but also as the active layer in photovoltaic cells [40–42] or artificial retinas [36, 43].

In this study, we investigate the performance of a range of microbial rhodopsin proteins in the MISM architecture. By choosing a representative protein from the thermophilic bacterium *Thermus thermophilus* living in hyper thermophilic condition (*i.e.,* around 75°C), Thermophilic rhodopsin (TR) [44, 45], we succeeded in increasing the operational temperature range of our devices to 70°C, while simultaneously increasing the device's responsivity and speed by an order of magnitude. Combining those results with a pH dependent investigation of a PD based on bacteriorhodopsin BR, the well characterised model rhodopsin protein functioning as a light-driven proton pump [46, 47], the photocurrent parameters could be correlated with aspects of the protein's photocycle. The obtained correlation was further used to gain understanding of the properties of a novel halide (*e.g.,* Cl^- and SO_4^{2-}) pumping rhodopsin protein *Synechocystis* halorhodopsin *Sy*HR [48]. Finally, we discuss the use of differential photodetection for the study of photoactive proteins, and the potential of photoactive proteins to provide suitable active layers in the MISM device architecture, also considering potential secondary functionalities, such as pH or temperature sensitivity.

2 Materials and methods

2.1 Protein expression and purification

2.1.1 TR and *Sy*HR

TR and *Sy*HR were prepared using essentially the same procedures as previously described (see [49] for TR and [48] for *Sy*HR). In short, the chemically synthesized TR or *Sy*HR gene was heterologously expressed in *Escherichia coli* BL21(DE3) cells, as recombinant proteins with a six-histidine tag at the C-terminus. Protein expression was induced by the addition of 1 mM isopropyl β-D-1-thiogalactopyranoside (IPTG, Wako Pure Chemical Industries, 99.9+%) and 10 μM all-*trans*-retinal (Sigma-Aldrich Co. Ltd., ≥98%). TR or *Sy*HR was then solubilized from the crude membrane fraction through the addition of *n*-dodecyl-β-D-maltoside (DDM, Dojindo, ≥98.0%). The solubilized proteins in DDM micelles were further purified by Ni^{2+}-NTA affinity chromatography and stored in a fridge in buffer solution (for TR: 50 mM tris(hydroxymethyl)aminomethane (Tris)-HCl, 1 M NaCl, 0.05% DDM, pH 7.0, for *Sy*HR: 10 mM 3-morpholinopropanesulfonic acid (MOPS)-NaOH, 300 mM Na_2SO_4, 0.05% DDM, pH 6.0) before use.

For the photocurrent measurements in the chosen MISM device architecture, films of proteins needed to be deposited on a substrate and covered with an insulating liquid medium (here buffer solution). In the case of films of protein in DDM micelles, their low adherence to the substrate and subsequent almost instant dissolution into the liquid medium resulted in a comparably weak photocurrent signal, along with an initially large dark current – likely related to the dissolution of the protein film (see Supplementary Figure S1). To increase the affinity of the protein film and hamper dissolution, proteins were reconstituted into lipid membranes, either consisting of L-α-Phosphatidylglyglycerol (PG, AVT) or L-α-Phophatidylcholine (PC, AVT), with a molar ratio of protein:lipid of 1:30, ensuring enough lipids surrounding the proteins for structural integrity, while keeping the density of the proteins high. To achieve reconstitution, PG or PC lipids were added to the protein-DDM sample together with Bio-beads SM-2 (Bio-Rad, 1523,920) at a concentration of 1 g per 10 mL of 0.1% DDM solution to adsorb the non-ionic DDM molecules. The reconstituted TR or *Sy*HR samples were washed with a buffer containing 50 mM Tris-H_2SO_4 (pH 7.0) or 10 mM MOPS (pH 6.0, 300 mM Na_2SO_4), respectively and stored at - 20°C as a pellet after centrifugation.

2.1.2 BR in PM

Expressed and purified samples of wild type BR in purple membrane (PM) obtained from *Halobacterium Salinarum* were kind gifts from AG Schlesinger (FU Berlin, Germany) [50]. Samples were stored in sodium azide, preventing the highly concentrated BR PM solutions from getting mouldy, which was removed prior measurements through washing in MQ water. BR PM was finally stored as concentrated pellets after washing with 10 mM MOPS-NaOH buffer (pH 7.4) in the freezer or fridge in the dark.

2.1.3 Buffer exchange

When needed, the sample buffer was exchanged prior film deposition. For this, pellets of condensed protein (in PC or PG membrane or PM) were re-dissolved at least 3x in the targeted buffer solution, homogenised and condensed using centrifugation, before

final dissolution and homogenisation. In the case of BR in PM, it became evident that aside from ensuring a relatively low room temperature during deposition (below 20°C) the resting time of the solution prior to film deposition (and thus the equilibrium of the solution's components) was decisive for the film's homogeneity as well as the prevention of cracks and the minimisation of coffee rings in the film, therefore prolonged equilibration times of the solutions were ensured. To avoid the formation of a thick salt layer on the protein films, dilute buffer solutions (10 mM MOPS or 25 mM Tris) were preferentially used without salt.

2.2 $M_cI_bS_pM_a$ device fabrication

The photocurrent performance of the protein films was studied using the $M_cI_bS_pM_a$ device architecture, either in the on-tip on-dip, planar or stacked architecture, depending on the measurement requirements (see Figure 1A). While the on-tip on-dip architecture allows the easy exchange of insulating buffer solution I_b, the planar architecture allows highly controlled studies with non-transparent counter electrodes M_c and the stacked architecture a close and well-defined electrode spacing between the active electrode M_a and M_c. For the planar architecture, electrodes strips of 2×26 mm were separated by 4 mm gap. For the stacked architecture the bulk electrodes were separated by a 1 mm thick glass spacer (allowing the comparably easy removal of the liquid medium) bonded using thermally curable spacers (60 μm, 110°C, Solarex). In the case of the temperature-dependent studies, a sealed device architecture was used to minimize evaporation of the I_b layer upon heating. For this, the bulk M_a electrode was covered with a film of 500 nm parylene-c around the active layer deposition site, into which the protein film was subsequently deposited as usual. A patterned Au electrode was used as M_c, and adhered onto the parylene-c film using the above mentioned thermally curable spacers. After filling with the I_b solution, the device was sealed with a glue gun.

2.2.1 Electrode deposition (M_a and M_c)

Either prefabricated thin films of indium tin oxide (ITO) on glass were used as M_a or 100 nm gold films (Tanaka, 99.99% or Lesker, 99.999%) on a thin adhesion layer of chromium (<25 nm) Au-Cr or a self-assembled monolayer Au-SAM (using 3-aminopropyltrimethoxysilate (APTMS, Sigma-Aldrich, >98%) and 3-mercaptopropyltrimethoxysilane (MPTMS, Sigma-Aldrich, >95%) in a 1:1 ratio, following essentially the procedure described in [51], deposited by physical vapour deposition (UPC-260, ULVAC Kiko. Inc., or KJLC Nano 36, Kurt J Lesker, rate 0.2–0.3 Å/s). Test experiments were also performed using 100 nm thick silver (Nilaco, 99.9+%) and copper (Nilaco, 99.99+%) electrodes with and without a chromium adhesion layer. However, compared to Au or ITO, especially the Cu electrodes were not robust against corrosion (see Supplementary Figure S2) induced by the ions in the protein films or buffer solution, and the lipid protein films were poorly adhered to the Ag electrodes, leading to a comparably weak signal and large dark-current, related to the slow peeling of the protein film.

In the case of the counter electrode M_c, transparent ITO electrodes or perforated Au electrodes were used in the stacked device architecture for BR/*Sy*HR and TR, respectively. Equivalent metal electrodes were used in the planar architecture (with patterned electrodes), and the stainless steel ferrule of the optical fibre was used in the on-tip on-dip measurement setup.

2.2.2 Protein film formation (the S_p layer)

Protein films were deposited onto substrates using drop coating from a range of buffer solutions. To ensure film homogeneity and smoothness, the uniform and soft vacuum of a water pump was used for the drying process. Other deposition parameters, such as temperature or equilibration time, were optimised when necessary (see also Section 2.1.3). Unless otherwise stated, 50 μL of protein in solution of fixed OD were used, resulting in films of about 10 mm diameter and thicknesses in the 5–10 μm range, with roughness values below 2 μm. After film formation, films were stored in a dry dark place until measurement.

In the case of BR-PM it should be noted that a reversible blue-shifted colour change could be observed in the films, upon prolonged drying. The concomitant appearance of a shoulder around 630 nm in the absorption spectrum of the film (see further Supplementary Figure S12) resembled the changes observed when lowering the pH value of the solution. This visible blue-shift could also be observed on films rehydrated in buffer solutions of pH 4.5.
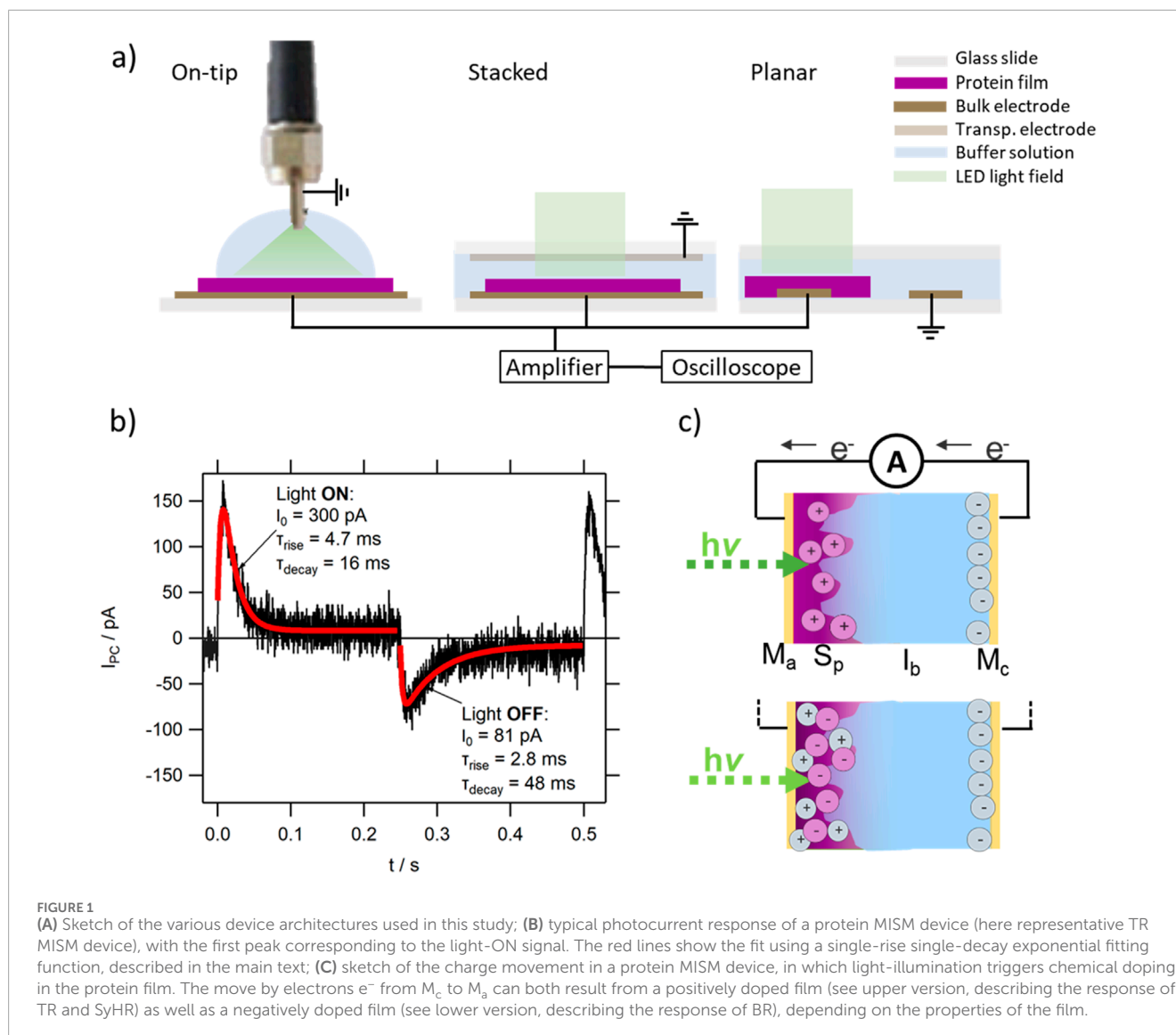
2.2.3 Insulating layer (I_b)

To ensure that the proteins could undergo the required structural changes upon illumination and to prevent denaturation, buffer solutions containing a range of components were used as I_b. 50 mM Tris-HCl or Tris-H_2SO_4 (Wako, 99.9%, pH 7.0), as well as 10 mM MOPS (TCI, >98%, pH 4.5–8.0) with or without NaCl, NaBr or Na_2SO_4 were chosen due to their good buffering performance.

I_b was placed onto the dried protein films. When needed, the I_b layer could be easily removed from the protein films by tilting the glass substrates onto an absorbing tissue (as the wetting of the film as well as that of the gold or ITO substrates was comparably low). No visible changes in the absorbance upon repeated rehydration could be observed, confirming the high stability of the protein films. Before adding a chemically different I_b layer, the film was washed with MQ water, to remove residual ions.

2.3 UV-Vis absorption spectroscopy – characterisation of protein solutions and films

UV-Vis absorption spectroscopy was used to confirm the purity and stability of the protein samples upon storage, buffer exchange and film deposition. The influence of salt type, salt concentration and pH on the absorption characteristics was also investigated, and results compared to literature. UV-Vis spectra were recorded on a Shimadzu UV-2450 or UV-3100 PC spectrometer in the range of 200–800 nm against buffer solution. In the case of reconstituted samples of TR and *Sy*HR, or in the case of BR PM, an integrating sphere was used to remove the effect of scattering.

The UV-Vis spectra of films on glass or ITO substrates were recorded through a perforated plate (d = 6 mm) fixed, normal to the beam, on the cuvette holder of the standard set-up of the UV-Vis

FIGURE 1
(A) Sketch of the various device architectures used in this study; **(B)** typical photocurrent response of a protein MISM device (here representative TR MISM device), with the first peak corresponding to the light-ON signal. The red lines show the fit using a single-rise single-decay exponential fitting function, described in the main text; **(C)** sketch of the charge movement in a protein MISM device, in which light-illumination triggers chemical doping in the protein film. The move by electrons e⁻ from M_c to M_a can both result from a positively doped film (see upper version, describing the response of TR and SyHR) as well as a negatively doped film (see lower version, describing the response of BR), depending on the properties of the film.

machine, against clean reference substrates. Due to the absorption of the ITO and glass substrates at wavelengths below 280 nm, no information in this spectral range could be obtained. UV-Vis spectra of selected films were measured on the day of film fabrication, after storing and rehydration, as well as before and after photocurrent measurements.

Where necessary, spectral deconvolution of the absorption spectra was performed using a combination of 3 log-normal curves following the strategy reported in [52].

2.4 Photocurrent measurements

Photocurrent measurements were performed, following the procedures described in [34, 53]. The modulated light of an LED of 530 nm was directed through a fibre optic cable ($d = 1$ mm, NA = 0.39) onto the active layer under study through a collimator, ensuring a distance-independent beam of about 5 mm diameter. The light power was regulated using a home-built setup and

calibrated using a commercial silicon photodiode. In the case of the on-tip on-dip measurement system, no collimator was used, resulting in a linear distance dependence of the diameter of the beam on the sample (see Supplementary Figure S3). The distance was optimized prior to measurement to ensure the illumination of a large (or the entire) area of the protein film. The frequency f_{light} of the square-wave modulated light was regulated by a function generator (Hewlett Packard 8116A or Texio FG-274). The measured transient photocurrent signals I_{PC} of the MISM devices were amplified using a low-noise transimpedance amplifier (Femto DLPCA-200, 10^8–10^9, DC mode, unless otherwise stated), and recorded on a digital oscilloscope (Tektronix TBS1052B or TDS5104B).

Each device was tested for time-dependency (long-term stability), as well as dependence on f_{light}. It is well established that upon increasing f_{light} the transient waveform changes to a square waveform (defined as 100% signal strength for bandwidth calculation [31]) and then a triangular signal, until the bandwidth f_{BW} of the device is reached and the light modulation speed exceeds

the speed of response of the MISM device. For comparison, most data were acquired at a modulation frequency low enough to allow sufficient discharge of the device during the light-OFF period.

2.4.1 Temperature dependence

For the temperature dependent measurements between RT and 75°C in 3–6 steps, sealed MISM devices were placed onto a Peltier heater (Adaptive), which was mounted on top of a heat sink to reduce hysteresis between heating and cooling curves. The effective device temperature dependence on applied voltage (PS-3020, Daiwa) was calibrated using the recorded temperature (thermocouple, Kaise, KU-2602) in a drop of glycerol on top of a glass slide with dimensions similar to the MISM device (see Supplementary Figure S4) which showed equilibration times below 3 min for moderate ΔT. To minimize the effect of the electric noise caused by the Peltier heating method on the quality of the photocurrent data, the device was equilibrated for 10 min, after which the DC power source was temporarily switched off and a photocurrent signal recorded. The repetition of the heating/cooling cycles showed equivalent results, as long as the evaporation of the I_b layer could be avoided.

2.4.2 Dependence on pH, salt concentration and salt type

The dependence of the photocurrent signal on pH (10 mM MOPS, 25 mM NaCl, pH 8.0, 7.4, 6.8, 6.2 and 4.5) was studied using freshly calibrated buffer solutions as I_b layer on the same protein film (see further Figure 7A). After each photocurrent measurement series, the I_b layer was carefully removed. The films were washed using MQ water by drop-casting a droplet and draining it at least 3 times, followed by a short drying under smooth vacuum for 5 min. If the on-tip on-dip method was used, the optical fiber tip was cleaned for reuse by washing 3x with ethanol. The stability of the protein film upon I_b layer exchange and time was confirmed by remeasuring the device performance at pH 6.8 before, during and after the pH dependent measurement series.

2.4.3 Fitting of I_{PC}

The analysis of the obtained I_{PC} traces follows the methodology previously published [53]. In short: The difference in amplitude between the light-ON and light-OFF peaks in I_{PC} was defined as the I_{pkpk} value, and was extracted directly from the data (deducting merely the noise). A single exponential rise and decay function was sufficient to fit the obtained I_{PC} traces (see Figure 1B):

$$I_{PC} = I_0 * \left(e^{-(t-t0)/\tau decay} - e^{(-(t-t0)/\tau rise)} \right) + I_{dc}$$

where I_0 is the amplitude, I_{dc} the dark current, τ_{rise} and τ_{decay} the lifetimes of the rise and decay of I_{PC}, respectively. The moved charge (i.e., the area underneath I_{PC}) was calculated from the fitting parameters: $Q_I = I_0 * (\tau_{decay} - \tau_{rise})$.

Unless otherwise stated, in all photocurrent data $I_{PC}(t)$ displayed here, the first peak corresponds to light-ON. In all devices, the counter electrode M_c was grounded, and therefore a positive peak in the light-ON signal corresponds to the movement of electrons from M_c towards M_a in the eternal circuit, with the consecutive formation of the negative component of the electric double layer (EDL) at the I_b/M_c interface (see Figure 1C).

2.4.4 Wavelength dependence

For the wavelength dependent measurements in the range between 400–700 nm, a home-built action spectrum set-up was used, previously described for organic MISM devices [53]. In short: the light of a tungsten/halogen light source (Spectral products, ASBN-W 100 L) was transmitted through a monochromator (Digikröm CM110, 1.2 mm grating – 10 nm resolution or 2 mm grating 15–20 nm resolution) modulated using a light chopper at a sample-dependent frequency (42 Hz TR and BR, 3–6 Hz SyHR) and focused through a pinhole of 2 mm diameter using a set of 2 achromatic lenses onto the device. The device was connected through a transimpedance amplifier (Femto, DLPCA-200) to a lock-in amplifier (NF Corporation, 5610B or PerkinElmer 7265 DSP) against the reference signal provided by the chopper. The signal magnitude $I_{dev, lock}$ was recorded through a digital multimeter (Keithley 2,110 5 1/2) using a home-written labview program, which allows the recording of several back and forward scans at chosen parameters. To reduce noise and to account for the comparably low bandwidth of the devices, a long time-constant at low modulation speed was chosen (after optimisation of the signal), and the measurements were performed with Δλ = 1 or 2 nm, Δt = 5–10 s. To improve the signal-to-noise ratio, several (back and forward) scans were averaged – after ensuring no significant change with measurement time or scanning direction.

In all cases a stacked device architecture was used. In the case of BR and SyHR, a transparent ITO electrode was used as M_C, through which the device was illuminated. The counter electrode was separated from the M_a electrode by spacers of about 0.9 mm thickness, allowing the filling and exchange of buffer solutions for studying the pH dependence. In the case of TR, the same stacked device architecture as for the temperature dependent measurements was used, thus illumination happened through an electrode free area on the glass used to hold the M_c electrode.

The recorded wavelength dependent $I_{dev, lock}(\lambda)$ spectrum was further converted into a responsivity spectrum (see also Supplementary Figure S8) $R_{dev}(\lambda)$ to remove the influence of the wavelength dependent input light-intensity $P_{light}(\lambda)$. For this, the light-intensity was calibrated using a silicon photodiode, with known responsivity spectrum $R_{SiPD}(\lambda)$, prior to measurement under identical conditions (i.e., through a ITO electrode, if that has been used as counter electrode in the device).: $R_{dev}(\lambda) = I_{dev, Lock}/P_{light} = I_{dev, Lock}/I_{SiPD} * R_{SiPD}$. As I_{dev} is not identical to I_{pkpk} obtained by the photocurrent measurements (due to the transient nature of the device, which affects the output signal of the lock-in amplifier in a non-trivial manner), only information about the shape of the wavelength dependent spectrum was considered for analysis. To improve S/N ratio in the data, and thus enhance signal quality for data comparison, a smoothing function was used where necessary.

2.5 Impedance studies

The equivalent circuit of liquid systems must be described using a combination of capacitive and resistive components [54]. This leads to a frequency dependent complex impedance, with the magnitude Z(f) and the phase shift θ(f), between the real component Re(Z) (f) = Z(f)cos(θ(f) π/2), the resistance, and the

imaginary component Im(Z) (f) = Z(f)sin(θ(f) π/2), the reactance of the system.

The frequency dependent impedance Z(f) and θ(f) of the electrolytic buffer solutions used for I_b were studied between two parallel bulk ITO electrodes (40[1] x 9 mm), separated by a spacer of 4 × 1 mm (sealed with the above mentioned thermally curable spacers) within the range of 4 mHz–100 kHz in 100 steps (on the log scale) using a home-written labview program to control the LCR Meter ZM2371 with ZM2392 low-impedance test leads (NF corp., speed vslow, voltage 100 mV, trigger delay 1s), after correcting for contributions of the cables and electrodes. The dependence of the curves on the concentration of NaCl or Na_2SO_4 was measured through titration of a concentrated salt solution in a 4 mL UV cuvette (filled with 3.5 mL solution) in the range between 0 and 1 M in several steps on the log scale. The dependence on pH was measured for buffers of 10 mM MOPS with and without 10 or 25 mM NaCl or 12.5 mM Na_2SO_4 within the pH range of 4.9 – 8.2, confirmed prior measurement using a pH meter (Seven Compact, Mettler Toledo). The LCR ITO electrodes were washed with DI water and ethanol, and dried before exchanging the sample medium. For the temperature dependent measurements in selected I_b (25 mM NaCl, with and without 10 mM MOPS), the cuvette was placed in an oil-bath on a stirrer hotplate, which was equilibrated for 10 min between measurements (using a stirrer) in the range between 20°C and 70°C in 5°C–10°C steps (both heating and cooling cycles), after degassing the sample through centrifugation to avoid the formation of air bubbles during the heating process.

2.5.1 Fitting of the impedance spectra

For fitting the obtained impedance spectra, a common equivalent circuitry has been used [55], which contains the minimal electrical components to fit the obtained data and which considers that not all of the listed components show a visible effect on the data in the frequency range studied (see Figure 2A). The equivalent circuit contains: (i) a constant phase element[2] (CPE), to describe the behaviour of the formed electric double layer CPE_{EDL} (ii) a resistive element[3] to account for the electronic contacts and cables R_{ec} and (iii) a parallel circuit of a resistor with a capacitor, to describe the bulk liquid, C_{bulk} and R_{bulk}. As can be seen in Figure 2B, the model used can obtain good fits for representative measured Z(f) and θ(f) curves.

For systems in which $R_{bulk} \gg R_{ec}$ (as in our case), R_{bulk} determines the height of the plateau region visible in Z(f) at moderate frequencies, if $C_{EDL} \gg C_{bulk}$. Only at elevated frequencies (beyond our measurement range) does Z(f) decay to R_{ec} (the onset of this decay is visible in the $Z_{DIwater}$(f) curve in Figure 2B). The low

frequency impedance is mostly determined by the electric double layer constant phase element CPE_{EDL}, where the non-ideality value n, can be obtained by the difference in θ(f→0) and the purely capacitive theoretical phase of 90°. For all our data, the main contribution of the CPE_{EDL} is capacitive (with n values between 0.96 and 0.98), and thus a frequency dependent EDL capacitance of C_{EDL}(f) = 1/(2πf*Im(CPE_{EDL})) will be defined for comparison. The bulk capacitance C_{bulk} can, in our system, be consistently approximated to be below $C_{bulk} \approx 65$ pF, and is only in very dilute solutions visible, determining the rise of the θ(f) curve at higher frequencies. It should be noted that for most traces, only an upper limit of C_{bulk} can be obtained due to the upper frequency limit of 100 kHz of our setup.

To allow setup independent comparison of the data, the resistivity ρ_{bulk} (in Ω cm) and the capacitance per unit surface area cs_{EDL} (in F/cm^2) are used. The ability to extract values through geometrical considerations of the measurement cell has been confirmed (see Supplementary Figure S10): $\rho_{bulk} = R_{bulk}$ A/L, and $cs_{EDL} = C_{EDL}$/A (where A corresponds to the area of the electrode in the solution, and L to the distance between the parallel electrodes).

2.6 Light-induced pH change

The light induced pH changes of a suspension of *E. coli* cells expressing *Sy*HR were studied depending on the wavelengths of light and salt content. For this, the cultured *E. coli* cells were washed three times in a solution containing 300 mM NaCl or 100 mM Na_2SO_4 to remove residual culture medium and resuspended in the same solution until OD_{660} = 7. pH changes were monitored using a LAQUA F-72 pH meter equipped with a micro ToupH electrode (Horiba Ltd., Japan) at 25°C controlled by a thermostat. Each cell suspension was kept in the dark, followed by a 3 min long illumination with a 300 W Xe light source MAX-302 (Asahi Spectra Co. Ltd., Japan) through bandpass filters of either 400 ± 10 nm or 520 ± 10 nm. Measurements were repeated under identical conditions after the addition of the protonophore carbonyl cyanide-*m*-chlorophenylhydrazone (CCCP, final concentration, 10 μM) and further addition of tetraphenylphosphonium (TPP$^+$, final concentration, 20 mM).

3 Results and discussion

3.1 TR MISM devices

The incorporation of TR as the photoactive layer S_p in the differential MISM photodetector resulted in a clear photocurrent response, with responsivity improved by an order of magnitude compared to the devices reported in 2015, based on *Sr*SRI [34] (see Figure 3A). This can be partly explained by the improved overlap between the used LED and the absorption maximum of TR at 530 nm, which gives TR in solution, as well as in the deposited films, a characteristic pink appearance. Furthermore, TR has been reported to be a proton pump of comparably high efficiency and of high thermal stability (in 2014 TR was record holder with stability over 3 h at temperatures as high as 75°C [45]).

---

1 Note, this value depends on the amount of liquid used (see below and Supplementary Figure S10).

2 Although in [55], the EDL is described as a combination of a pure capacitor and a CPE, the data did only show very faint traces of the pure capacitor, with $C_{EDL} \sim C_{CPE}$ values, and thus this complication has been omitted for clarity.

3 The contribution of a coil element has been omitted, as it is mostly associated with the cables, and this dependence should have been removed through the corrections before the measurements.
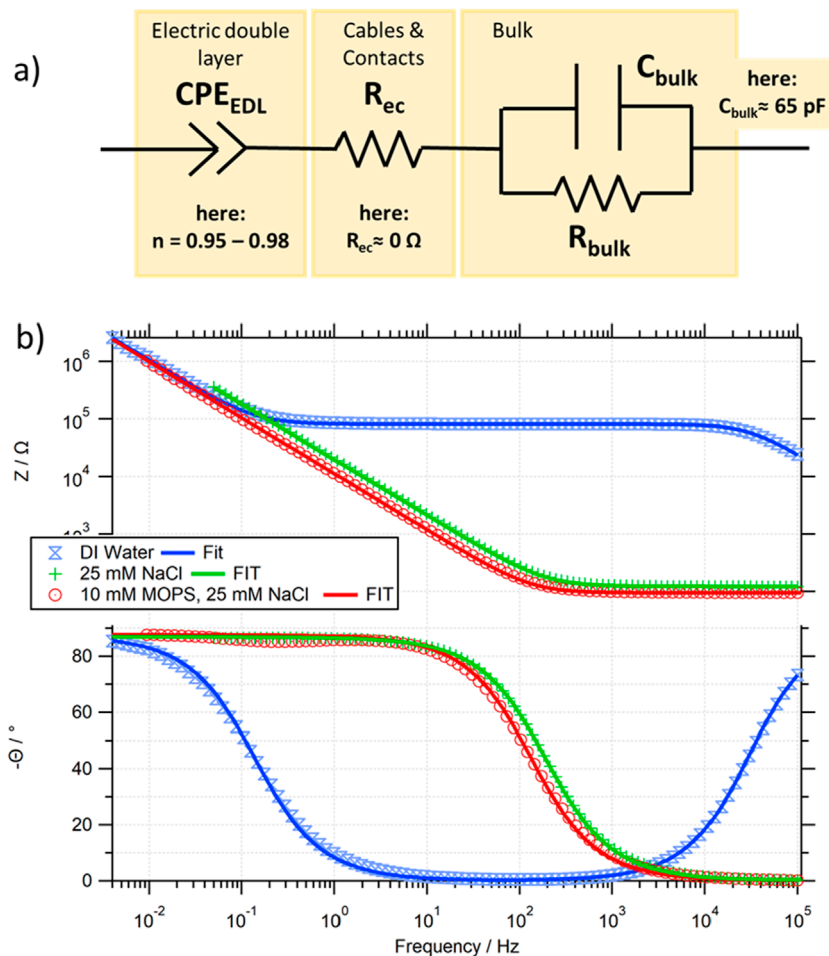
FIGURE 2
(A) Equivalent circuit used for the fitting of the experimentally obtained impedance spectra; **(B)** comparison of the experimental data and calculated fit based on **(A)** for pure water (blue), a salt (green) and buffer (red) solution.

The magnitude of I_{PC}, as well as its high stability with time, allowed the conductance of a full characterisation of the TR MISM response. The characteristic MISM PD frequency dependence of I_{PC} can be observed, reaching bandwidths f_{BW} exceeding the 100 Hz range (see Figures 3C, D) depending on the exact device architecture. The rise and decay of I_{PC} could be well fitted with the introduced single exponential rise and single exponential decay function (see Figure 1B), with τ_{decay} in the 10s of ms and τ_{rise} in the ms range. It should be noted that the rise time is already affected by the rise of our amplifier, therefore discussion will be mostly limited to the decay times. When comparing the light-ON and light-OFF peaks, it becomes evident that τ_{decay} is lower under illumination, with concomitant increase in amplitude I_0, leading to a balanced charge Q_I being moved back and forth during the light-ON-OFF cycles.

For organic MISM devices, the τ values could be associated with the resistive and capacitive elements in the equivalent circuit [32]: The photovoltage source in the S layer V_S could be shown to be in series with a resistor R_S, corresponding to the active layer, followed by a capacitive element C_S of the S layer, connected in parallel with the series R_I and C_I elements, as well as R_{ec} corresponding to

the insulator and the electronic connections, respectively. Although the interpretation of R_S and C_S is not trivial for protein films (especially in the case that no charge-transfer but chemical doping of the film occurs), as would be the assignment of Fermi levels (found essential for the description of the polarity of response in organic MISM devices [53]), certain aspects of this model will be considered and terminology of it used, before considering the effect of the photocycle kinetics of the proteins under light illumination. According to the model [32], the total series resistance $R_S + R_I + R_{ec}$ strongly affects the signal magnitude, while both τ values are associated with the RC time constants of the parallel circuits, i.e., $(R_S + R_I + R_{ec})^*C_I$ and $R_x^*C_S$, with R_x being the smaller of R_S or R_I. The amount of charge $Q = Q_S + Q_I$ stored internally in the organic device is directly proportional to the sum capacitance of the layers $Q = V_s^*(C_S + C_I)$. In contrast, for a chemically doped film, the effective charge Q_S should determine the photovoltage V_S (through $V_S \sim Q_S$), responsible for charging I_b capacitor C_I: $Q_I = V_S^*C_I \sim Q_S^*C_I$, thus being proportional to the charge of the protein film, and likely to increase with protein layer thickness. The time-constant associated with the charging of the S layer in organic MISM devices, is likely to be not only related to the electronic components of the S_p layer, but
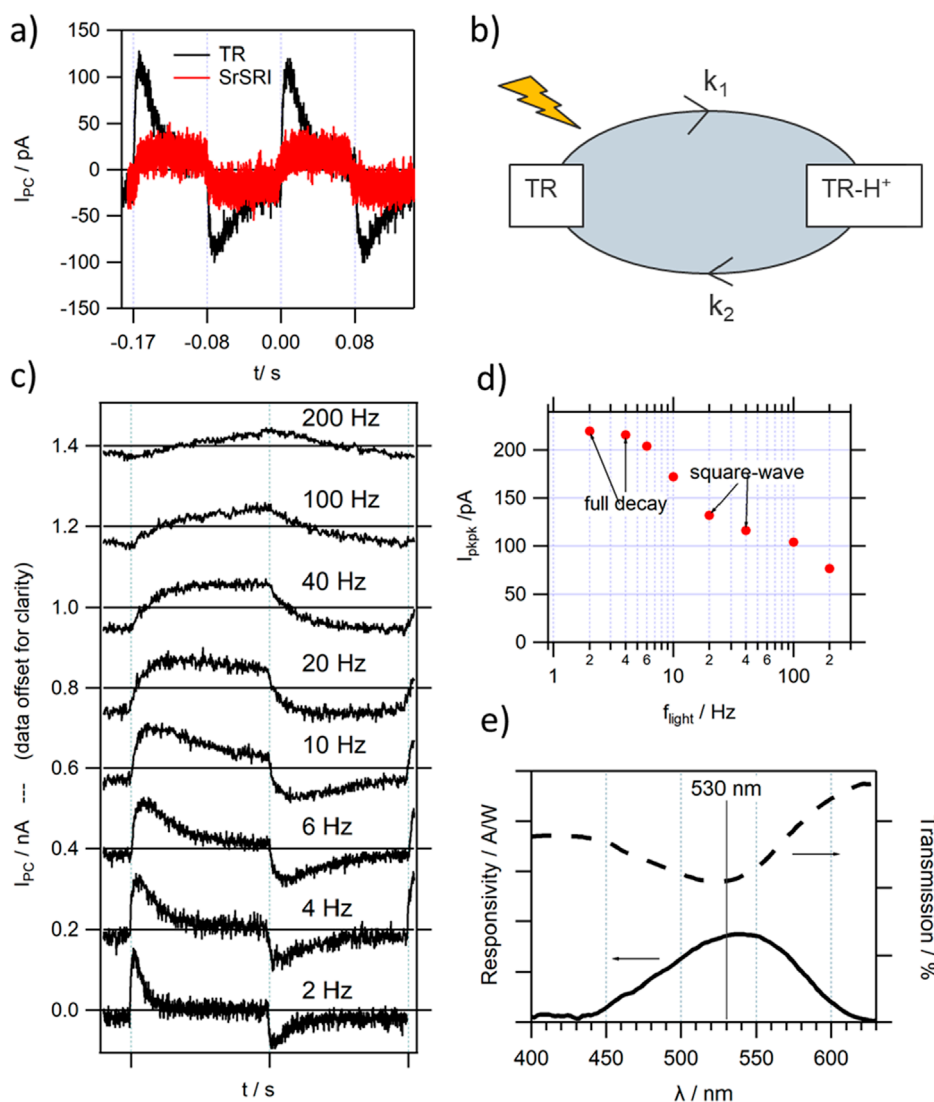
FIGURE 3
Photocurrent response of a typical TR MISM device **(A)** comparison with a device based on SrSRI [34]; **(B)** sketch of the reduced photocycle of TR, resulting in a positively charged film upon light illumination; **(C)** dependence of I_{PC} on the modulation frequency of light f_{light} (data offset by 0.2 nA for clarity); **(D)** extracted I_{pkpk} vs. f_{light} from **(C)**; **(E)** wavelength dependent responsivity of a TR based device in comparison to the transmission spectrum of TR.

also of the kinetics of the charging process itself (influenced by the time constants k_1 and k_2 as illustrated, *e.g.*, in Figure 3B) (*vide infra*).

Consistent with previously reported data on organic MISM devices [34], the signal intensity increased asymptotically, when increasing the salinity of I_b, and therefore reducing the resistance in the active layer R_I (see Supplementary Figure S5). A similar increase could be obtained upon increasing the salt content in S_p during film deposition. However, this hampered homogeneous film formation and led to a lower stability of M_a even for the relatively inert Ag. In general, salt was therefore added to I_b and the film was deposited with the minimum amount of salt required for ensuring protein stability. Concomitantly to the increase in I_{pkpk} the speed of the PC response increased (and thus τ decreased, as expected from a reduction in R_I or R_S). The speed did (as expected) also increase when decreasing the thickness

of the S_p layer (see Supplementary Figure S6). Simultaneously, however, I_{pkpk} was reduced, likely due to the reduced number of TR proteins in the film, and a possible increase in C_s, lowering V_s.

Furthermore, the characteristic sub-linear light intensity dependence of MISM devices [32, 53] could be observed. However, in contrast to devices having an organic S layer, no significant changes in signal shape with increasing light intensity could be observed (see Supplementary Figure S7), within the resolution of the TR I_{PC} traces, suggesting that the electronic parameters (R and C), or the corresponding lifetimes τ, are not affected by the increasing number of charges within the protein film [32], and the sublinearity of the increase in responsivity with increasing light intensity can be directly correlated with a reduced charging efficiency of the S_p layer.

As can be seen in Figure 2E, the wavelength dependence of the photocurrent response for the TR MISM device shows a high overlap with the absorption spectrum of TR, confirming the that optical activity of TR is the primary reason for the observed photocurrent signal. The slight red-shift in the position of maximum responsivity to $\lambda_{Resp\_max} = 540$ nm could be a result of the strong linear increase in light power (towards longer wavelengths) of our light-source, and the associated even higher increase in the number of available photons for longer wavelengths.

The polarity of the photocurrent response corresponds to the negative component of the EDL building up at the I_b/M_c interface (see Figure 1C upper case). The photocycle of TR [44] consists of a number of intermediate states with corresponding rate constants k_i. In two of these transitions, a proton is either moved in or out of the TR protein moiety. For TR it has been reported that photoactivation results first in a proton uptake, followed by a proton release [44], as illustrated in Figure 3C. Under constant illumination protons would thus accumulate in the TR film, inducing a positive doping of the S_p layer, drawing negative charge to M_a via the external circuit, and counterbalancing the negative polarity of the EDL at M_c. Whether or not the doping leads to any charge transfer between the active metal M_a and adjacent S_p layer cannot be extracted from our data. However, we have previously reported that in the case of dry films of SrSRI, the signal polarization could be inverted, essentially inducing an MISIM architecture, where the S_p layer is electronically separated through an additional insulating (here non-responsive protein film) layer [34]. In the case of organic films, the MISIM architecture prohibits any charge transfer from S to M_a, which greatly enhanced the speed of organic MISIM devices, compared to their MISM counterparts [56]. In the case of SrSRI, it was shown that under such conditions, the polarity of response can then rather be explained by the lower case depicted in Figure 1C, which will be further discussed when considering the BR photocell.

The good thermal stability of TR, also reported for elevated temperatures, facilitated a temperature dependent measurement of the photocurrent signal (see Figure 4). Upon increasing the operation temperature of the TR-MISM photocells gradually to 75°C, a linear increase in signal magnitude (I_{pkpk} and I_0) and a concomitant increase in signal speed was observed (see Figure 4C–lower trace). When comparing the values between RT and 66°C, I_0 increased linearly almost 3x, τ_{decay} decreased 5x, while τ_{rise} less than 2x. The quasi-linear decrease in τ can be explained by a power relationship of its corresponding rate constant $1/\tau$ with T (see Supplementary Figure S9), which strongly increases especially at elevated temperatures. The comparably small increase in I_0 compared to that in τ_{decay} results in a more then 2fold decrease in "moved" charge Q_I in the TR MISM device with T (see Figure 4C–middle trace), which could correspond to either an increase in insulating layer capacitance C_I or decrease in photovoltage V_S in the protein layer (and thus its accumulated charge Q_S).

In order to correlate the observed changes with the behaviour of the protein film and/or the photocycle kinetics of TR, the effect of temperature on the RC time constants of the buffer solution I_b needs to be considered and subtracted. Therefore, the impedance of the isolated I_b layer was studied in more detail using impedance spectroscopy.

3.2 The role of the impedance of the I_b layer on I_{PC}

The impedance spectra of the studied electrolyte or buffer solutions of moderate concentration, measured in the frequency range relevant for low-speed MISM devices with $f_{BW} <$ kHz, could be well described with the proposed equivalent circuit [32], composed of a parallel RC section, associated with bulk effects (according to the Debye model describing the bulk capacitance of the cell and the ionic conductivity in the bulk), a CPE related to the EDL and a resistor associated with the resistances of the electrical contacts and cables (see Figure 2).

3.2.1 Dependence on salt concentration

When increasing the salt concentration, the ionic conductivity in the bulk increases asymptotically from approximately 0 (0.055 for the ideal pure water solution [55]) to 3.7 mS/cm, seen in the inverse proportionality of the resistivity to the salt concentration (bottom trace in Figure 5A and Supplementary Figures S11a, S11b), related to the dissociation of the salt. For concentrations between 10 and 100 mM this leads to a decay in resistivity of about 73% ($\rho_{100mM} \approx 0.27\ \rho_{10mM}$), from 1.4 k$\Omega$ cm to 0.38 kΩ cm, respectively. The second electronic component in the equivalent circuit determining the response in this frequency range is the CPE associated with the EDL. While the frequency independent parameter Q decays slightly for concentrations above 100 mM (see middle trace in Figure 5A), n stays approximately constant at 0.972 (within the associated measurement error of 1%). This results in a slight exponential increase in the CPE equivalent capacitance per unit surface area cs_{EDL} at 200 Hz from 3.3 μF/cm² to about 4.3 μF/cm² at 1 M salt concentration (top trace in Figure 5A). Although the equivalent capacitance of the CPE is frequency dependent, the values do not differ dramatically. No significant change in behaviour could be observed when changing the salt from NaCl to Na_2SO_4. For all traces, we could approximate $cs_{bulk} \lesssim 35$ pF/cm² and $\rho_{ec} \approx 0\ \Omega$ cm (<< 270 Ω cm), confirming that those electrical components show negligible influence on the impedance in the frequency range of interest. The R_I and C_I parameters used in the model [32] to describe the MISM photocurrent response correlate, therefore, with R_{bulk} and C_{EDL}, respectively.

The strong but asymptotic decrease in ρ_{bulk} and only slight positive change in cs_{EDL} for higher salt concentration is consistent with the previously reported changes in MISM photocurrent response [34], as well as that observed for the TR MISM devices (see Supplementary Figure S5). Decreases in insulating layer resistance, and concomitant overall resistance of the MISM device, explain the observed asymptotic increase in I_{pkpk}, while both parameters will influence the RC time constants, which will decay faster compared to R_I, caused by the counterbalancing increase in C_I at high concentration (see Supplementary Figure S11b). When changing the geometry of our photocurrent cell, the R and C parameters of the insulating layer will change. We could show that R_{bulk} shows the expected purely geometric dependence on ρ_{bulk}, and thus increases with electrode distance L and decreases with electrode area A (see Supplementary Figure S10): $R_{bulk} \sim L/A$. In contrast C_{EDL} only depends on the width of the EDL and not the electrode spacing L and increases proportionally with A. Thus, RC ~ L, leading to a slower time constant with increasing electrode spacing, while I_{pkpk} should
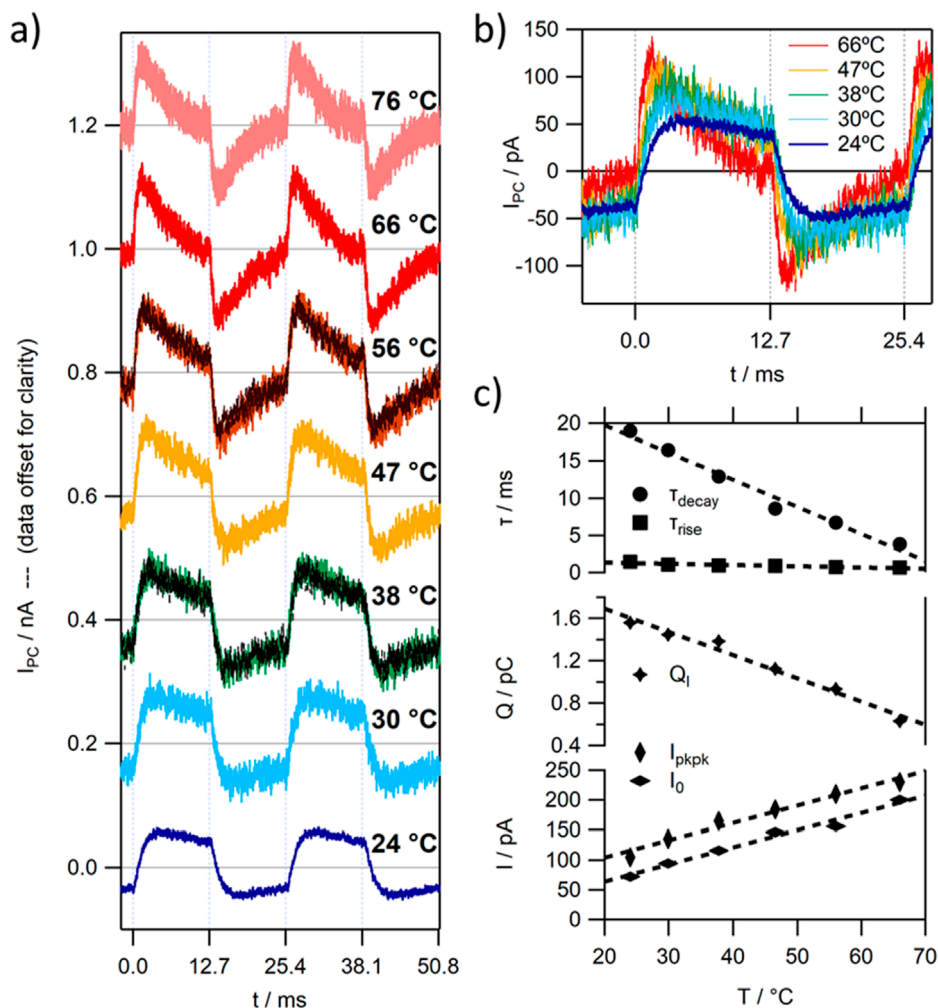
FIGURE 4
Temperature dependence of the photocurrent signal of a typical TR MISM PD; **(A)** I_{PC} at 39.3 Hz – data offset by 0.2 nA for clarity; **(B)** selected I_{PC} from **(A)** without offset; **(C)** fitting constants of the single exponential fit function of the light-ON peak vs. temperature.

decrease with electrode spacing and increase with illuminated area (consistent with our previously reported results [33]). While the situation is more complicated for the on-tip on-dip architecture, the overall trends should be similar.

3.2.2 Temperature dependence

In the next step, the influence of temperature on the solution's impedance spectra were investigated. Increases in temperature of an electrolyte solution can be associated with an increase in ion dissociation [57]. This can explain the slight exponential decay in ρ_{bulk} seen in the measured temperature dependent impedance spectra (see bottom trace in Figure 5B, or see ESI 11c for σ_{bulk}). Simultaneously, the EDL capacitance increases quasi linearly, through a linear decrease and concomitant increase in the frequency independent CPE parameters Q and n, respectively. This leads to a slight extenuated decrease of its corresponding RC time constant with T compared to ρ_{bulk} (see Supplementary Figure S11d) over a small range: $RC_{70C} \approx 85\% \; RC_{20C}$.

The slight changes in $R_I \triangleq R_{bulk}$ by 30% over the studied T range and the merely 15% decrease in $R_I C_I$, cannot explain the strong changes observed in τ_{decay} and I_0 in the photocurrent response of the TR MISM devices. The order of magnitude of the obtained $R_I C_I$ values lies in the ms range (or even below) close to the τ_{rise} values. This suggests that the rise of the PC signal could possibly be associated with the charging of the I_b layer, while the strong changes in τ_{decay} should be mostly related to changes in S_p.

As already mentioned, upon light illumination a photocycle is triggered in TR, which consists of several intermediates, all associated with their own rate constants k_i [44]. If light continuously illuminates such a protein (as happens during the light-ON period), some intermediates will accumulate. During one of those intermediates a proton is taken up by TR from the solution, forming a TR-H^+ complex, followed by a H^+ release at a later intermediate in the photocycle. The accumulation of intermediates involving the TR-H^+ complex can therefore result in a positive doping of the S_p layer, resulting in the movement of charge in the external circuit (see also
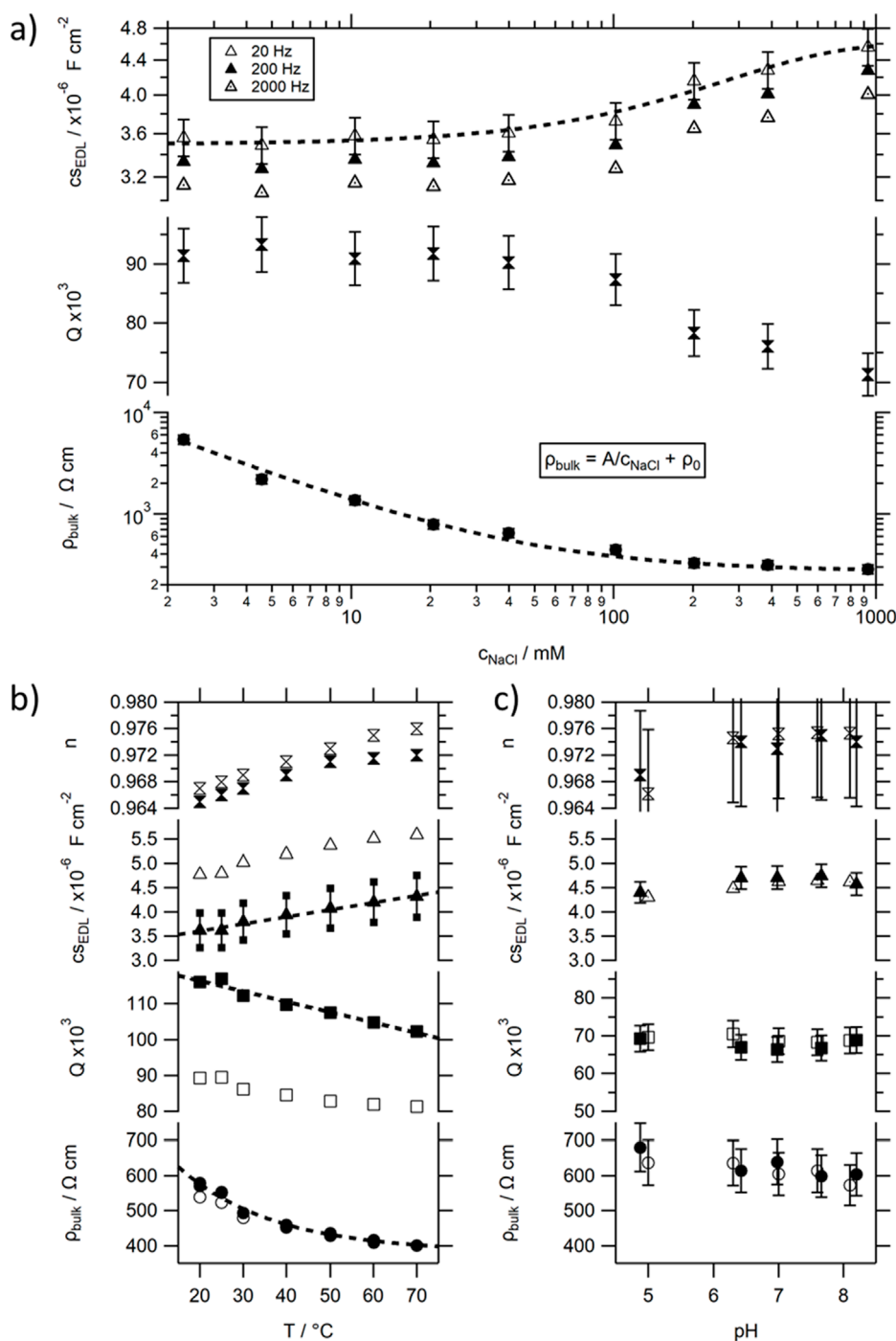
FIGURE 5
Values for the resistivity ρ_{bulk}, the frequency independent parameters n and Q of the CPE_{EDL} and its (at certain frequencies) calculated specific equivalent capacitance cs_{EDL} extracted from recorded impedance spectra of electrolytic solutions using the model introduced in Figure 2 and the M&M section. **(A)** dependence on salt concentration; **(B)** dependence on temperature; **(C)** dependence on pH.

Figures 3B, 3C). The amount of charge in the S_p layer, which would be counterbalanced by Q_I, depends on the balance between the rate constants k_1 and k_2 between the formation and decay of the TR-H$^+$ complex, as well as the probability of triggering a photocycle in the protein. We have seen that Q_I decreases with T, which could be either related to a decrease in C_I or V_S (caused by Q_S) driving the charge

movement between M_a and M_c. The observed 1.2 fold increase in C_I with T (see Figure 5A), would lead to a slight increase in Q_I. However, a more then 2fold decrease is observed, which should therefore be related to a decrease in Q_S. Using our simplified model depicted in Figure 3B, a decrease in Q_S would imply a greater balance in rate constants k_1 and k_2 and would also explain the observed

increased similarity in τ values between the light-ON and light-OFF peaks at elevated temperature.

The decrease in τ_{decay}, and concomitant strong increase in $1/\tau_{decay}$ should be associated with the rate constant k_{charge} of accumulating the charged equilibrium state of the doped film under illumination. This equilibrium state should be earlier reached, if the photocycle kinetics (and with them k_1 and k_2) increase. It was previously reported that the photocycling rate of TR increases strongly with increasing temperature (measured up to 80°C) [44], being thus optimised for efficient proton pumping activity at high temperatures as would be likely for proteins found in a thermophilic organism. This was also supported by the comparably large activation energy. The recovery of the original state (which influences k_2 in Figure 3B) increased about 20fold during an increase from RT to 50°C [44] from 3.6 s^{-1} ($\tau \approx 0.3$ s) to 69 s^{-1} ($\tau \approx 15$ ms).

3.2.3 pH dependence

The I_b layer in our protein MISM devices is not just an electrolyte solution, but a buffer solution. The general dependence on ion concentration, as well as temperature, observed in the impedance spectra are identical for a salt solution or a buffer solution (see $e.g.$, non-filled markers in Figure 5B). However, the addition of buffer to a sample, has 2 pronounced effects. Firstly, it decreases the bulk resistance, but less than would be expected by the equivalent addition of salt. And secondly it increases the frequency independent parameter n of the CPE, while simultaneously decreasing Q. This leads to an overall increase in C_{EDL} by about 30%, $i.e.$, by about the same change observed when going to a 1 M solution of salt.

It should be noted that a buffer solution is not only characterised by the concentration of its buffer or salt components, but also by its pH. The pH of a buffer is highly relevant for the activity of biomolecules due to its influence on the ionic state of a number of amino acids. Therefore, the influence of the pH on the impedance of the buffer solution was also tested (see Figure 5C). Within the tested frequency range, no significant influence on the impedance spectrum could be observed.

To understand this result, it is worth considering what happens during a pH change to the ions in a solution. As the pH is defined as pH = -log [H_3O^+], where [H_3O^+] is the hydronium ion concentration, its values display the concentration and activity of released hydrogen ions. pH values can theoretically go from 0 to 14, with the autodissociation constant of water K_w being set to K_w = ([H_3O^+][OH^-])/[H_2O] = [H_3O^+][OH^-] = 10^{-14} (at 25°C). Therefore, in a neutral solution of pH 7 both ions are present at 0.1 μM, while at acidic pH of 3 the concentration of hydronium ions would be increased to 1 mM and at the alkaline pH of 9 reduced to 1 nM. In all I_b layers used in this study, salt concentrations or concentration of buffer components exceed the 10 mM range, concentrations in which small changes to ion concentration are not causing significant changes in recorded impedance spectra. The slight observed changes with increasing pH, follow the trends of increasing salt concentrations. In this context it should be noted, that used buffer solution MOPS is acidic, with a pK$_a$ value of 7.2. Its optimal buffering range lies between pH 6 and 8. In order to obtain the desired pH values, sodium hydroxide (NaOH) was titrated to the solution, leading to an increase in the number of Na$^+$ ions

(and a concomitant decrease in the H$^+$ ions) with increasing pH. As a pH buffer can guarantee a constant pH once its buffering range is reached, even if [H$^+$] or [OH$^-$] are momentarily changed through external stimuli, through the partial dissociation of the buffering agents (HB↔H$^+$+B$^-$), supplying or withdrawing protons from the solution, considerable amounts of NaOH have to be added, to achieve the desired pH increase.

The observed slight decrease in ρ_{bulk} can thus be associated with the increase in Na$^+$ ions in the solution upon pH titration. However, its influence reduced compared to the dependence on the addition of NaCl, possibly related to the concomitant decrease in H$^+$ concentration. While visible, the changes are very small, and thus, any considerable changes in I_{PC} with pH in a protein MISM device should therefore be related to the changes in the S_p layer, and associated with the photocycle pathway and kinetics of the protein.

3.3 BR MISM devices

For TR, no information on the pH dependence of its photocycle kinetics is available, and therefore another well studied microbial rhodopsin protein Bacteriorhodopsin BR was chosen to study the dependence on pH on the photocurrent signal. Since its early discovery in 1971 [46], BR has evolved to a model protein for light-driven proton pumps, found in the membrane of microbes, fueling the synthesis of ATP. Its photocycle has been studied in great detail (see ref in [47]). In nature, BR occurs in the form of a two-dimensional hexagonal lattice of BR-trimers in the so-called purple membrane (PM), which is a distinct section within the cell membrane of the archae $Halobacterium$ $salinarum$, in which BR is the only protein present. BR in PM can be isolated directly from the Hs culture, leading to a comparably high rhodopsin concentration within the membrane (protein:lipid ratio approximately 3:1 [58]) compared to reconstituted samples (as used in the study of TR, SrSRI and SyHR), and thus resulting in a comparably high quantum yield of deposited films. However, the quantum yield at 530 nm is reduced by about 50%, due to a red-shift in the absorption maximum of BR towards 568 nm at ambient pH values (see Supplementary Figure S12) [59], compared to TR. For low pH, a purple to blue transition can be observed, related to the protonation of an amino-acid Asp85, located close to the Schiff base (SB) and the retinal chromophore. Asp85 acts in its deprotonated form as primary proton acceptor from the SB during the photocycle. The protonation of Asp85 at low pH, and thus the occurrence of a shoulder in the absorption spectrum of BR, located at around 600 nm (see Supplementary Figure S12), strongly reduces the light-induced proton transport [59]. The pKa of Asp85, with its value of approximately 2.6 [59], sets therefore the low limit of pH for BR functioning as a proton pump.

For BR featuring a deprotonated Asp85 a photocycle can be triggered by light absorption through the retinal chromophore which initialises proton translocation. This light induced proton translocation is known to be a multistep process driven by changes in the proton affinities ($i.e.$, their pKa values) of crucial amino acid side groups. In general, for pH below the pKa of the side groups ($i.e.$, pH with comparably high H$^+$ concentration in solution) the majority of amino acids are found in their neutral protonated state (A-H) or eager to receive a proton if being deprotonated by a

previous reaction, while for high pH values, the amino acids are deprotonated (A$^-$) or eager to deprotonate. In analogy to TR, two steps in the photocycle are crucial for the MISM applications, the first involving the proton release into the medium from a so-called proton release complex (PRC), and the second involving the proton uptake from the medium by an amino acid, Asp96 in the case of BR, featuring pKa values of 5.8 and 7.2–7.5 during the corresponding steps, respectively. Changing the pH of the surrounding medium has therefore pronounced effects, not only on the order of proton uptake and release, but also on the kinetics of the photocycle (see Figure 6) [59]: In the case of a pH ensuring a deprotonated PRC (or facilitating the deprotonation of the PRC) (*i.e.*, pH > 5.8), a proton is released from BR via the PRC to the solution at the extracellular side shortly after photoisomerization of the retinal. A slow proton uptake from the intracellular side follows before the activated protein fully decays to its original state (see left side in Figure 6). The rate of proton uptake (and thus k_2) is further slowed down upon increasing the pH above the pKa value of the proton acceptor Asp96 [59, 60]. In contrast, at pH below 5.8 (see right side in Figure 6), the slow proton uptake takes place before the unfavourable proton release, which nevertheless happens shortly after the proton uptake by Asp96 from the PRC-H complex, and thus the sequence is inverted, changing the charge of the light activated BR PM film from being negative to positive. The proton uptake can be further delayed (and thus k_1 decreased) when decreasing the pH below the pKa of an amino-acid (pKa$_{Asp35}$ = 4.5) which slows the required deprotonation of Asp96 by only slowly transferring its proton to the deprotonated SB, which is required prior to uptake of the proton from solution. It should be noted that conformational changes in the proteins, *e.g.*, the flip of Asp96 after deprotonation from an orientation facing the SB to one facing the cytoplasmic surface or relocation of mobile internal water molecules during transitions between photocycle intermediates ensure the directionality of the photocycle reaction [59].

As expected, a stable photocurrent response can be observed in BR MISM devices (see Figure 7B), along with their characteristic dependence on light illumination frequency associated with the differential device architecture (see Supplementary Figure S13). At pH ≥ 6.2, the device shows a positive light-ON peak, which increases in magnitude with increasing pH. The signal intensity observed at high pH values is increased compared to TR by another order of magnitude, likely due to the denser protein film, and fast I_{PC} response. The device bandwidth can approach the kHz range, and thus also increased by an order of magnitude compared to TR. This is consistent with the reported increase in photocycling rates of BR at room temperature being about 10-fold faster compared to TR, but similar to TR at elevated temperature [44]. The increase in I_{pkpk} with pH is accompanied with an increase in the τ_{decay} (see Figure 7C–top trace), while τ_{rise} remains stable, ensuring the pH independent bandwidth. It should be noted that an increase in τ_{decay} would concomitantly cause an increase in I_{pkpk} until the decay of I_{PC} is slow enough to not intercede its signal rise [32], explaining the steeper increase of I_{pkpk} with pH compared to I_0 (see Figure 7C–bottom trace). The simultaneous increase in peak height and width leads to a significant overall increase in charge Q_I moved between the electrodes for a given light signal (see Figure 7C–middle trace).
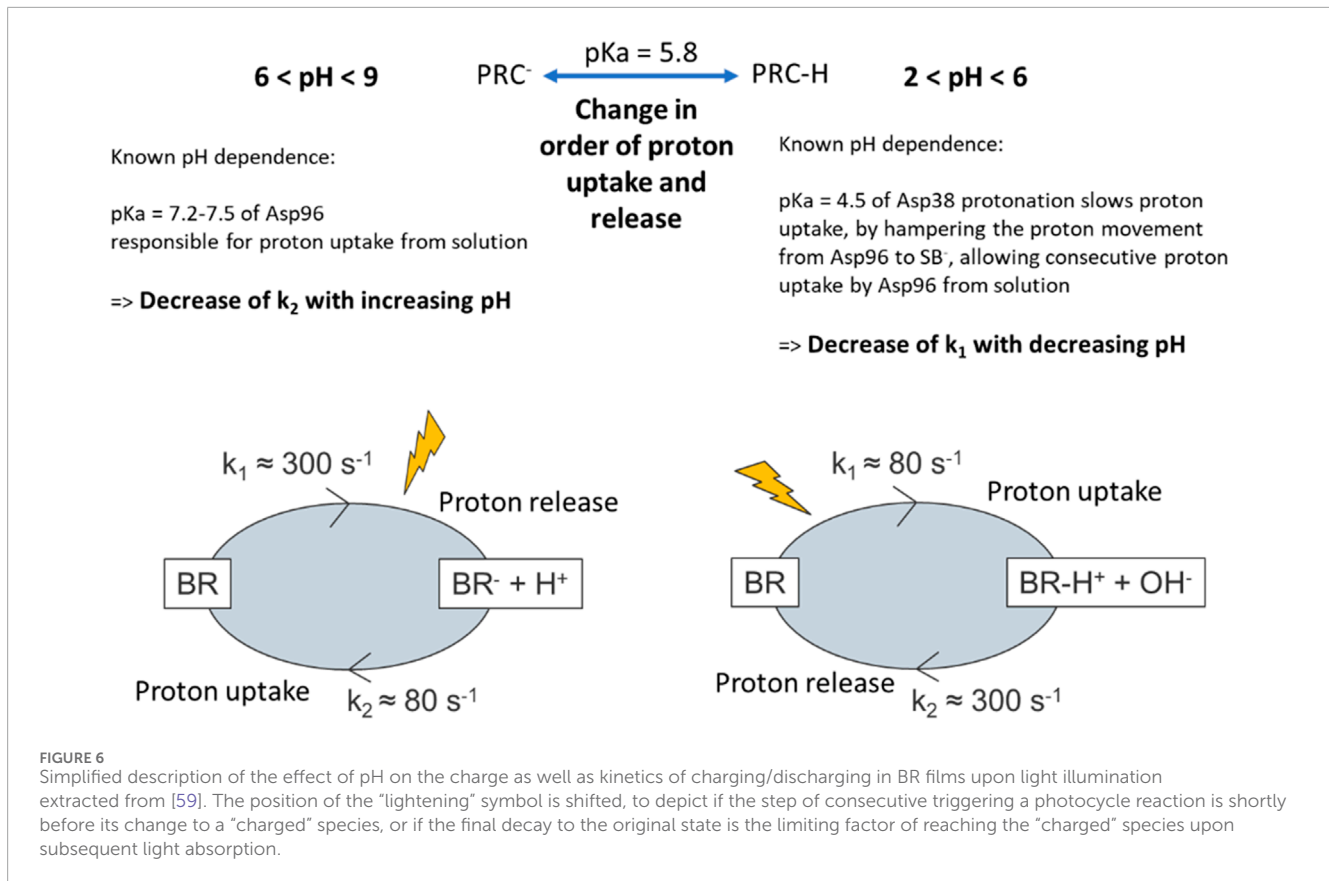
When lowering the pH below the critical value of 5.8 to, *e.g.*, 4.5, the polarity of the photocurrent signal is inverted (see Figure 7B

red trace). The observed signal inversion would agree with the reported change in the order of proton uptake and release [59]. The comparably low signal to noise ratio and large fluctuations at pH values below 5.8 hamper reliable characterisation of its I_{PC}. However, it can be seen that the bandwidth of the PC signal is significantly reduced, caused by an increase in τ_{rise} which approaches the value of τ_{decay}. When considering τ_{rise}, its sudden increase for low pH values seems surprising considering the almost constant $R_I C_I$ values of the I_b layer, obtained from the impedance studies (see Figure 5C). However, the rise can only be rate limited by the comparably fast reacting I_b layer, if k_1 (or the contribution to k_1 happening directly after light illumination, which is most of it, in the case of low pH values – illustrated in the position of the "lightening" in Figure 6) is faster than the I_b response. This can be the case for BR at elevated pH, but at low pH the initial charging of the BR film happens with slow kinetics. In such a case, the increase in charge in the S_p layer controls both the rise and decay of the PC signal. Furthermore, the comparably fast k_2 does not control the time of reaching an equilibrium state under illumination, leading to close values for τ_{rise} and τ_{decay}, as observed in the I_{PC} traces. This would decrease the measured Q_I values, and also is consistent with the observed large discrepancy between I_0 and I_{pkpk}.

At elevated pH the increase in τ_{decay} with pH agrees with a slowing of the overall photocycle kinetics, caused by a reduction in k_2, as discussed before. The greater imbalance in τ_{decay} to τ_{rise} leads to an increase in induced charge in the BR PM film at equilibrium state. However, it should be considered that the BR film at a specific pH value consists of a mixture of states, determined by the balance in protonation state of some amino acids (according to their pKa values). At pH 6.2, already a significant percentage of BR molecules will feature a protonated PRC group, locally inverting the induced charge of the film. This would attenuate the light induced Q_S of the equilibrium state at pH values approaching 5.8, and would add to the decrease in Q_I associated by the changing photocycle kinetics. This also explains, why in some cases close to the pKa value of the PRC only an unstable signal can be observed, featuring double-peak behaviour–known also from organic MISM devices, in which two competing processes occur [53].

In contrast to the shape of I_{PC}, the shape of the wavelength dependent photocurrent does not change with pH within the full measurement range (see Figure 7D). The spectrum overlies well with the absorption spectrum of BR at elevated pH values. The appearance of the shoulder peak in the absorption spectrum at low pH values (around 630 nm) is not visible in the wavelength dependence photocurrent spectra. This confirms that blue shifted BR does not contribute to proton translocation, as reported previously [59], and thus has no photocurrent activity. The partly purple to blue transition of BR will therefore be another factor contributing to the observed reduction in I_{PC} observed at low pH values by deactivating some of the BR proteins from proton pumping.

While the change in polarity upon decreasing the pH value below 5.8 can be easily explained by the reversal of the proton uptake and release steps in the BR PM film, the observed photocurrent polarity is contradictory to that observed for TR MISM devices. A negatively doped film would be expected to induce a positive charge in the M_a layer by moving e$^-$ to M_c, resulting in a negative light-ON peak (see Figure 1C, upper case). However, in the case of BR a

FIGURE 6
Simplified description of the effect of pH on the charge as well as kinetics of charging/discharging in BR films upon light illumination extracted from [59]. The position of the "lightening" symbol is shifted, to depict if the step of consecutive triggering a photocycle reaction is shortly before its change to a "charged" species, or if the final decay to the original state is the limiting factor of reaching the "charged" species upon subsequent light absorption.

positive peak is observed. As already mentioned, a second scenario can be used to explain the direction of charge movement between the electrodes (see Figure 1C, lower case): here, the released ions would stay in the protein film, close to the M_a electrode, drawing charge of opposite polarity to that obtained in the solution (and not the proteins). We can only speculate on the reason this might occur in BR PM films, which could include their greater density, or a lower ability of water molecules to move in and out of the film. The unified orientation of BR molecules in the PM membrane (in contrast to the "random" orientation in reconstituted samples) and the thereby unidirectional light-activated H^+ translocation could be another reason.

3.4 *Sy*HR MISM devices

In the next step, we aim to investigate factors affecting the photocurrent response of MISM devices, based on a novel microbial rhodopsin protein, *Sy*HR [48]. Interestingly, *Sy*HR was the first reported microbial rhodopsin protein which supposedly transports divalent ions, despite their large size. The device would, therefore, allow an investigation of the influence of valency and ion size on the photocurrent response, when comparing I_{PC} in the presence of Cl^- or SO_4^{2-} ions.

As can be seen in Figure 8A, a positive photocurrent peak upon illumination with green light can be observed in the presence of Cl^- ions in *Sy*HR MISM devices. The characteristic change in shape with f_{light} can already be seen at comparably low

light modulation frequencies with f_{BW} in the 10 Hz region (see Supplementary Figure S14), and thus about an order of magnitude slower than those obtained for TR. The magnitude of I_{PC} is similar to that of TR at high pH values, and increases 2fold when decreasing the pH in the solution (see Figure 8B– bottom trace) (in contrast to BR, where a strong decrease of I_{pkpk} is observed with decreasing pH). By analogy to BR, we see a strong increase in τ_{decay} with increasing pH (see Figure 8B– top trace), however, the extracted values are in average about 5x larger. This suggest comparably slow photocycle kinetics in *Sy*HR compared to BR. At pH values below 7.0 *Sy*HR shows similar rate constants compared to TR at RT. The very slow decay of the photocurrent peak especially at elevated pH values, results in large Q_I values (see Figure 8B– middle trace), about 10 to 20x those measured for TR, or for BR at low pH values. Only at pH 8.0 does Q_I measured for BR exceed the values of *Sy*HR, due to the considerably increased magnitude in BR's PC response.

During the photocycle a Cl^- release from a binding site close to the retinal chromophore has been reported to occur, with a subsequent Cl^- uptake at a later intermediate of the photocycle [48] (illustrated in Figure 8D). This would result in a positive doping of the protein film, drawing e^- to the M_a electrode, as evident by the positive PC peak upon light illumination. Therefore, a similar model as used for TR can be used to explain the polarity of PC response. The same polarity (as expected by the conserved order in anion release/uptake [48]), but for a much weaker (about 2 orders of magnitude) photocurrent response can be observed when exchanging Cl^- for SO_4^{2-} ions in the I_b solution (see Figure 8C). It was previously reported that performance of
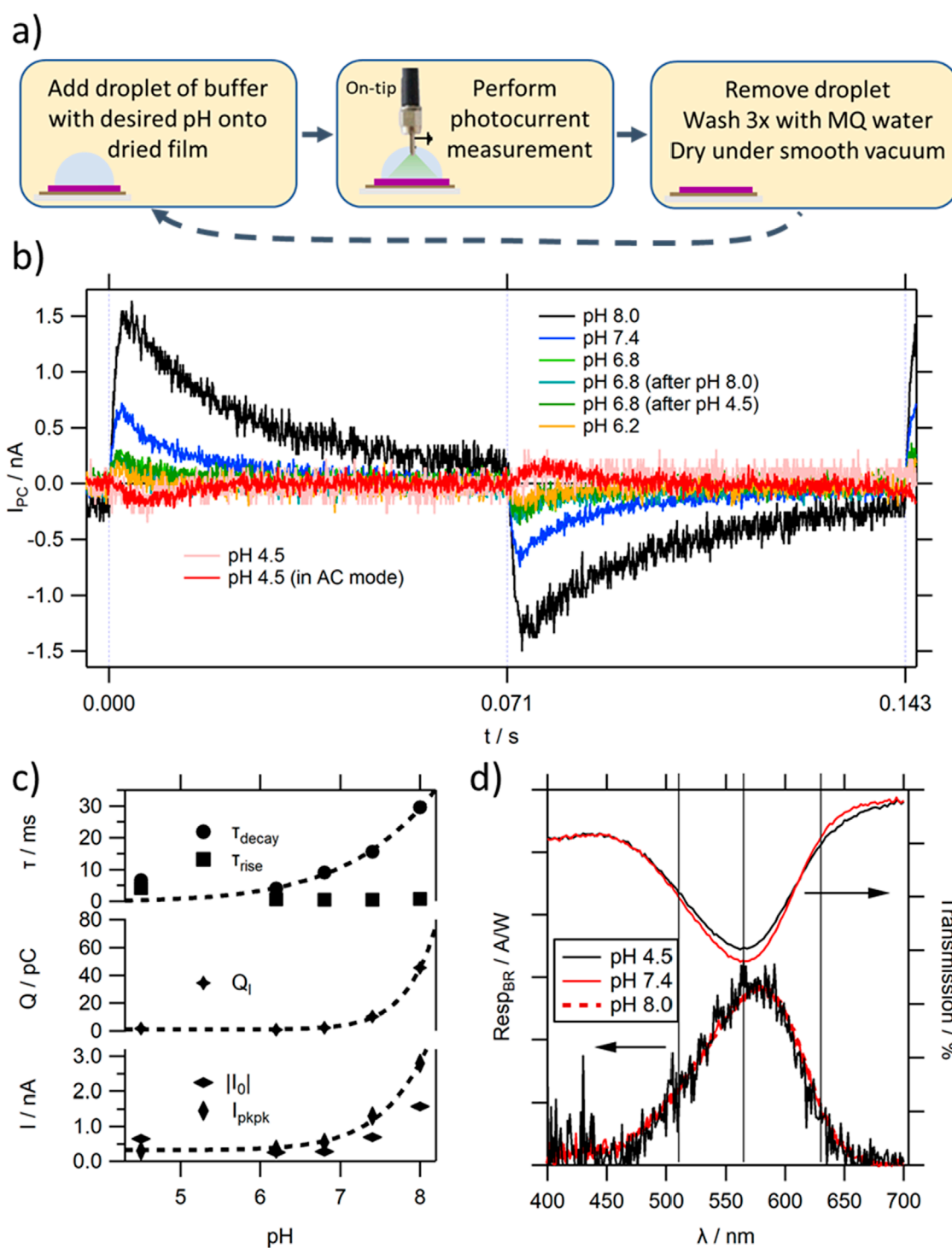
FIGURE 7
(A) Process flow of pH dependent photocurrent measurements; **(B)** photocurrent response at a light modulation frequency f = 7 Hz of a selected BR MISM device depending on pH (at pH = 4.5 the trace is also shown in AC mode for clarity); **(C)** fitting parameters extracted from the light-ON photocurrent response shown in **(B)**; **(D)** wavelength dependence of the photocurrent response of a BR MISM device for different pH values. The respective transmission spectra of BR are shown for comparison. The lines show the positions of the 3 peaks underlying the transmission spectra (see also Supplementary Figure S12).

SO_4^{2-} pumping by *Sy*HR is comparably low [48], which would be consistent with the low responsivity of our devices. The strong decay in I_{pkpk} is accompanied by an about 10fold increase in τ_{decay}, suggesting very slow photocycle kinetics in the presence of SO_4^{2-} ions. As both ions have an influence on the absorption maximum of its deeply buried retinal chromophore, compared to
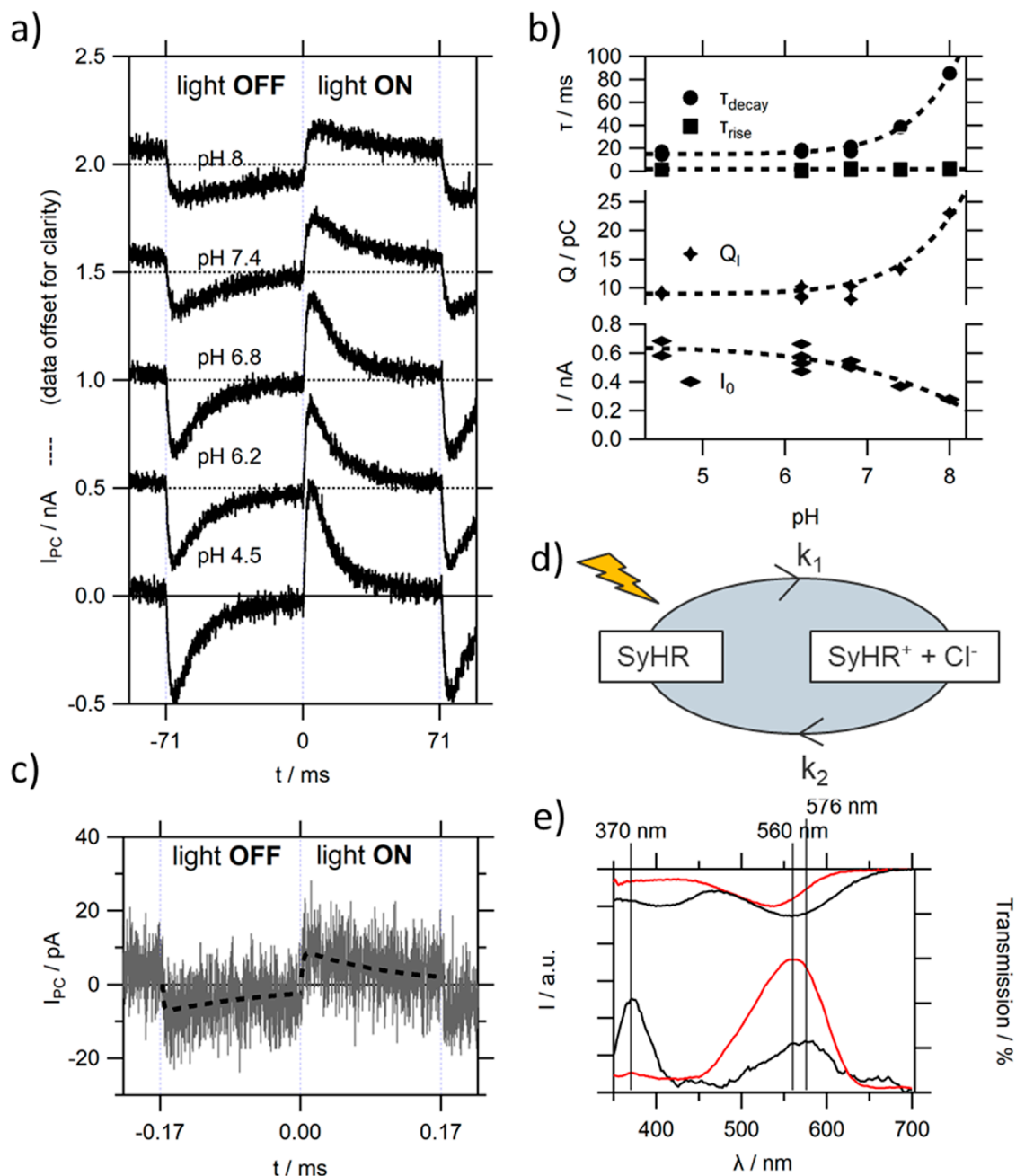
FIGURE 8
(A) The influence of pH on I_{PC} of a representative SyHR MISM device in the presence of Cl⁻ ions in the I_b solution; **(B)** extracted fitting parameters of **(A)** for the light-ON peak; **(C)** I_{PC} recorded in the presence of SO_4^{2-} ions (without Cl⁻). The dashed line represents the single rise single decay fit of the data; **(D)** simplified model of photocycle of SyHR, resulting in a positively charged film under light illumination; **(E)** dependence of SyHR MISM devices on the wavelength of light illumination, in the presence of Cl⁻ (red trace) and SO_4^{2-} ions (black trace). The top traces correspond to the respective transmission spectra.

that reported in salt free solution, an anion binding site close to the retinal chromophore has been suggested [48]. Thus, the observed slow kinetics of moving a large ion deeply into the SyHR moiety compared to a small ion seems consistent with this understanding.

When measuring the wavelength dependence of the photocurrent response (see Figure 8E) in the presence of

Cl⁻ ions a strong peak can be observed with a maximum at 560 nm slightly red-shifted compared to the absorption spectrum (see also Supplementary Figure S15). The position and shape of the wavelength dependence does not change with pH in the solution.

In the case of SO_4^{2-} the wavelength dependent photocurrent spectrum features 2 peaks, one at 575 nm and the other at 370 nm.

The peak at 575 nm can be expected, and agrees with the 20 nm red-shift in the absorption spectrum upon binding of SO_4^{2-} ions (see Supplementary Figure S15) [48]. It should be mentioned that a second peak around 400 nm has been reported for elevated pH values in the absorption spectra of *Sy*HR in the presence of both Cl^- and SO_4^{2-} ions. This peak has been attributed to the deprotonation of the SB in *Sy*HR, with pKa values of 10.6 in the presence of Cl^-, which is lowered to 8.2 in the presence of SO_4^{2-} [48]. However, these values were measured for *Sy*HR in DDM micelles. In the case of *Sy*HR reconstituted into PC lipid membranes, the pKa of this transition seems to have dramatically decreased in the presence of SO_4^{2-} ions (see Supplementary Figure S15). Upon addition of Cl^- ions to the solution, the peak disappears, and the main peak resembles that measured in pure Cl^- solutions, showing that *Sy*HR has a much larger affinity to Cl^- compared to SO_4^{2-} ions, and suggesting that the exchange to SO_4^{2-} facilitates the deprotonation of the SB even at moderate pH values.

Although no full characterisation of the PC behaviour at 370 nm could be made with our current setup, we could verify that the polarity of the PC peak remains positive upon blue light illumination. The observation of the comparably strong peak for blue light, inspired the wavelength dependent investigation of the light-induced pH changes of *Sy*HR in *E. coli* cells, depending on halide ion type. Upon blue light irradiation a light-induced pH decrease was observed in a solution containing only SO_4^{2-} ions, which disappeared through the addition of the protonophore, CCCP. This could suggest an initial proton uptake during the photocycle of *Sy*HR under blue light illumination, which would agree with the positive photocurrent response observed during the acquisition of the wavelength dependent photocurrent spectrum. In the presence of Cl^- ions, this activity was greatly suppressed. It should be noted that a similar H^+ pumping activity upon blue light illumination (above 360 nm) was reported in the Cl^- pump HR by [61]. A more thorough investigation of the origin of the peak, ideally combining measurements on photocycle kinetics upon blue light illumination with FTIR data providing information of the protonation state of crucial amino acids, would be, however, necessary to confirm this preliminary data.

Furthermore, the relative high ratio of peak height at 370 nm in the wavelength dependent photocurrent spectrum, compared to that at 576 nm corresponding to the pumping of SO_4^{2-}, might be misleading. A strong change in τ values of the corresponding I_{PC} traces, can considerably falsify relative $I_{peak, lock}$ values due to the use of the integrating lock-in amplifier in the measurement setup. The lock-in amplifier would generally generate larger values for square wave signals compared to transient ones (of similar magnitude). Simultaneously, the I_{pkpk} value of the square wave signal would be reduced compared to its lower frequency response. Therefore, a detailed study on I_{PC} under blue-light illumination should be included in a follow-up study.

4 Conclusions and outlook

4.1 The use of rhodopsin in PD

Building on the first demonstration of a microbial rhodopsin MISM photodetector in 2015 [34], the observation of a stable

photocurrent signal could be extended to three additional microbial rhodopsin proteins TR, BR and *Sy*HR. In all cases, the performance of photodetection was greatly improved, compared to the prototype *Sr*SRI MISM device, allowing detailed studies under a range of conditions. As expected, the wavelength dependent responsivity of the devices did well align with the corresponding absorption spectra of the protein films. Furthermore, the changes in the kinetics of the decay of the photocurrent peak (τ_{decay}) followed the changes in photocycle kinetics reported in previous studies. Although the bandwidth of the protein MISM devices are still low compared to MISM devices based on optimised organic semiconductors (despite the increase from the 10 Hz to kHz range upon changing from *Sy*HR to BR), the order of magnitude of the device's responsivity (reaching 5 µA/W and 2 µA/W, for BR and *Sy*HR PD at their respective absorption maximum when calculated at full decay, respectively), the specific detectivity (approx. 1×10^6 cm $Hz^{1/2}$/W and 3×10^4 cm $Hz^{1/2}$/W, for BR and *Sy*HR, respectively) as well as their f_{BW} approach those observed for low mobility organic semiconductors [62].

The extraction of protein film dependent rate constants from our devices is facilitated by the nearly constant electronic parameters of the I_b layer with pH and temperature, featuring comparably low time constants which barely influence the shape of I_{PC}. Nevertheless, the extraction of photocycle kinetics from I_{PC} data would require a combination with spectroscopic techniques, providing detailed information of the state of the protein film, and should be combined with an investigation of the effect of induced electric fields on photocycle lifetimes of the film in equilibrium as well as during device operation. Furthermore, although it could be shown that the polarity can be inverted when changing the chemical doping of a given protein film with *e.g.*, pH, the direction also depends on the model which needs to be used for the interpretation of the results, which greatly depends on the film condition, as has been already shown for our prototype devices [34].

4.2 The use of proteins in MISM devices to add additional functionalities

Using proteins instead of organic semiconductors provides us with the possibility of adding secondary functionalities to our MISM devices. As has been shown, if the proteins can considerably change their photocycle kinetics and/or the order of ion uptake or release, depending on external conditions other than wavelength of light, I_{PC} of the corresponding MISM device will also change. If a significant change in one of the parameters extracted from the I_{PC} curves can be obtained (as observed here for changes in pH or T, for τ_{decay}, I_{pkpk} and/or their combination *i.e.*, Q_I), the devices could be calibrated for each condition. This calibration also benefits from the reported quasi-insensitivity to the exact content of the I_b layer in respect to *e.g.*, ion or buffer concentration, once a few mM of ions are present in the solution. Once inserted into an I_b of *e.g.*, unknown pH or T, the obtained I_{PC} or extracted parameters could provide information about the pH or T, respectively.

4.3 The use of PD for the study of rhodopsin

The study on *Sy*HR, has also shown that the investigation of I_{PC} using the MISM device architecture of a novel protein, can provide suggestions on the influence of external parameters on the photocycle response and associated kinetics. Compared to common experiments used in the characterisation of photoactive biomolecules, the MISM experiment is simple and fast, and could thus be used to provide an initial screening tool of the biomolecules. Furthermore, when considering the information obtained upon increasing the temperature, it should be noted that those are only limited to the range of ensuring liquid buffer solutions. In contrast, if the proton pumping activity of rhodopsin proteins is measured in a living cell (*e.g.*, in the membrane of *E. coli*), a considerably narrower temperature range can be measured (ensuring intact cells) [63, 64]. pH dependent experiments are also limited to relatively natural pH values, while no limitations to the pH values are given in MISM devices.

Especially, once the understanding on the effect of an electric field across the MISM device on the photocycle kinetics has increased and a methodology developed allowing the reliable extraction of relevant values of photocycle kinetics from the rates obtained from the I_{PC} trace, the use of screening will increase for gaining understanding of the proteins themselves. In future it might also be used, in combination with other methods, to gain an improved interpretation of the (electro)chemical potential [65] of the proteins in the presence and absence of light.

Data availability statement

The raw data supporting the conclusions of this article will be made available by the authors, without undue reservation.

Author contributions

Funding

Conflict of interest

The authors declare that the research was conducted in the absence of any commercial or financial relationships that could be construed as a potential conflict of interest.

Publisher's note

All claims expressed in this article are solely those of the authors and do not necessarily represent those of their affiliated organizations, or those of the publisher, the editors and the reviewers. Any product that may be evaluated in this article, or claim that may be made by its manufacturer, is not guaranteed or endorsed by the publisher.

Supplementary material

The Supplementary Material for this article can be found online at: https://www.frontiersin.org/articles/10.3389/fphy.2024.1481341/full#supplementary-material

References

1. Balzani V, Credi A, Venturi M *Molecular devices and machines: a journey into the nanoworld*. Weinheim: Wiley VCH (2003).

2. Ciamician G The photochemistry of the future. *Science* (1912) 36(926):385–394. doi:10.1126/science.36.926.385

3. Spanggaard H, Krebs FC A brief history of the development of organic and polymeric photovoltaics. *Solar Energy Mater Solar Cells* (2004) 83(2–3):125–46. doi:10.1016/j.solmat.2004.02.021

4. Becquerel AE On electron effects under the influence of solar radiation. *Compt Rend Acad Sci* (1839) 9:561.

5. Chapin DM, Fuller CS, Pearson GL A new silicon p-n junction photocell for converting solar radiation into electrical power. *J Appl Phys* (1954) 25:676–7. doi:10.1063/1.1721711

6. Schmela M, Blume ST, Sauaia RL, Marques RF, Rau D, Buchet M, et al. (2022) Solar power europe (2022): global market outlook for solar power 2022-2026.

7. Agrell E, Karlsson M, Chraplyvy AR, Richardson DJ, Krummrich PM, Winzer P, et al. Roadmap of optical communications. *J Opt* (2024) 18(6):063002. doi:10.1088/2040-8978/18/6/063002

8. Ren H, Chen JD, Li YQ, Tang JX Recent progress in organic photodetectors and their applications. *Adv Sci* (2021) 8(1):2002418. doi:10.1002/advs.202002418

9. Oliveira J, Brito-Pereira R, Gonçalves BF, Etxebarria I, Lanceros-Mendez S Recent developments on printed photodetectors for large area and flexible applications. *Org Electronics* (2019) 66:216–26. doi:10.1016/j.orgel.2018.12.028

10. Long MS, Wang P, Fang HH, Hu WD Progress, challenges, and opportunities for 2D material based photodetectors. *Adv Funct Mater* (2019) 29:19. doi:10.1002/adfm.201803807

11. Fukuda K, Yu K, Someya T The future of flexible organic solar cells. *Adv Energy Mater* (2020) 10:25. doi:10.1002/aenm.202000765

12. Zhang YQ, Ma Y, Wang YX, Zhang XD, Zuo CT, Shen L, et al. Lead-free perovskite photodetectors: progress, challenges, and opportunities. *Adv Mater* (2021) 33:e2006691. doi:10.1002/adma.202006691

13. Ludin NA, Mustafa NI, Hanafiah MM, Ibrahim MA, Teridi MAM, Sepeai S, et al. Prospects of life cycle assessment of renewable energy from solar photovoltaic technologies: a review. *Renew and Sustainable Energy Rev* (2018) 96:11–28. doi:10.1016/j.rser.2018.07.048

14. Mooney M, Nyayachavadi A, Rondeau-Gagné S Eco-friendly semiconducting polymers: from greener synthesis to greener processability. *J Mater Chem. C.* (2020) 8(42):14645–64. doi:10.1039/d0tc04085a

15. López-Fernández I, Valli D, Wang CY, Samanta S, Okamoto T, Huang YT, et al. Lead-free halide perovskite materials and optoelectronic devices: progress and prospective. *Adv Funct Mater* (2024) 34:6. doi:10.1002/adfm.202307896

16. Tang CW Two-layer organic photovoltaic cell. *Appl Phys Lett* (1986) 48:183–5. doi:10.1063/1.96937

17. Zhu L, Zhang M, Xu J, Li C, Yan J, Zhou G, et al. Single-junction organic solar cells with over 19% efficiency enabled by a refined double-fibril network morphology. *Nat Mater* (2022) 21(656):656–63. doi:10.1038/s41563-022-01244-y

18. Hong G, Gan XM, Leonhardt C, Zhang Z, Seibert J, Busch JM, et al. A brief history of OLEDs-emitter development and industry milestones. *Adv Mater* (2021) 33:e2005630. doi:10.1002/adma.202005630

19. Rose S *The chemistry of life*. 3rd ed. London: Penguin Books (1991).

20. Alberts B, Johnson A, Lewis J, Raff M, Roberts K, Walter P *Molecular biology of the cell*. 5th ed. New York: Taylor and Francis Group (2008). Garland Science.

21. Schaechter M, Ingraham JL, Neidhardt FC *Microbe: Das Original mit Übersetzungshilfen*. Heidelberg: Spektrum Akademischer Verlag (2006).

22. Hanefeld U, Hollmann F, Paul CE Biocatalysis making waves in organic chemistry. *Chem Soc Rev* (2022) 51(2):594–627. doi:10.1039/d1cs00100k

23. Govorunova EG, Sineshchekov OA, Li H, Spudich JL Microbial rhodopsins: diversity, mechanisms, and optogenetic applications. In: RD Kornberg, editor, 86 (2017). p. 845–72. doi:10.1146/annurev-biochem-101910-144233 *Annu. Rev. Biochem.*

24. Kojima K, Shibukawa A, Sudo Y (2020) The unlimited potential of microbial rhodopsins as optical tools biochemistry 59: 3, 218–29. doi:10.1021/acs.biochem.9b00768

25. Ernst OP, Lodowski DT, Elstner M, Hegemann P, Brown LS, Kandori H Microbial and animal rhodopsins: structures, functions, and molecular mechanisms chem. *Reviews* (2014) 114(1):126–63. doi:10.1021/cr4003769

26. Palczewski K Chemistry and biology of vision. *J Biol Chem* (2012) 287(3):1612–9. doi:10.1074/jbc.R111.301150

27. Donner K, Yovanovich CAM. A frog's eye view: foundational revelations and future promises. *Semin Cell and Developmental Biol* (2020) 106:72–85. doi:10.1016/j.semcdb.2020.05.011

28. Dalgleish L, Dalgleish S, Singh A (2021) Radiation detector. European Patent application nb: WO2021032507-A1, Priority date: 21.08.2019, International publication date: 25.02.2021

29. Hu L, Noda Y, Ito H, Kishida H, Nakamura A, Awaga K Optoelectronic conversion by polarization current, triggered by space charges at organic-based interfaces. *Appl Phys Lett* (2010) 96:242303. doi:10.1063/1.3454915

30. Li B, Noda Y, Hu L, Yoshikawa H, Matsushita MM, Awaga K Highly efficient organic optoelectronic conversion induced by electric double layers in ionic liquids. *Appl Phys Lett* (2012) 100:163304. doi:10.1063/1.3697988

31. Dalgleish S, Matsushita MM, Hu L, Li B, Yoshikawa Y, Awaga K Utilizing photocurrent transients for dithiolene-based photodetection: stepwise improvements at communications relevant wavelengths. *J Am Chem Soc* (2012) 134(30):12742–50. doi:10.1021/ja304228c

32. Reissig L, Dalgleish S, Awaga K A differential photodetector: detecting light modulations using transient photocurrents. *AIP Adv* (2016) 6(1):015306. doi:10.1063/1.4939921

33. Dalgleish S, Reissig L, Hu L, Matsushita MM, Sudo Y, Awaga K Factors affecting the stability and performance of ionic liquid-based planar transient photodetectors. *Langmuir* (2015) 31(18):5235–43. doi:10.1021/la504972q

34. Dalgleish S, Reissig L, Sudo Y, Awaga K On-tip photodetection: a simple and universal platform for optoelectronic screening. *Chem Comm* (2015) 51(91):16401–4. doi:10.1039/C5CC06237C

35. Vsevolodov NN, Poltoratskii VA Holograms in biochrome, a biological photochromic material. Zh. Tech. Fiz. (USSR). 55: 10, 2093–2094. English translation: sov. *Phys — Tech Phys (Usa)* (1985) 30(10):1235.

36. Wagner NL, Greco JA, Ranaghan MJ, Birge RR Directed evolution of bacteriorhodopsin for applications in bioelectronics. *J R Soc Interf* (2024) 10:20130197. doi:10.1098/rsif.2013.0197

37. Pfeifer K, Ergal I, Koller M, Basen M, Schuster B, Rittmann SK-MR Archaea biotechnology. *Biotechnol Adv* (2021) 47:107668. doi:10.1016/j.biotechadv.2020.107668

38. Hampp N, Popp A, Brauchle C, Oesterhelt D Diffraction efficiency of bacteriorhodopsin films for holography containing bacteriorhodopsin wildtype BR(WT) and its variants BR(D96N). *J Phys Chem* (1992) 96(11):4679–85. doi:10.1021/j100190a098

39. Hampp N Bacteriorhodopsin as a photochromic retinal protein for optical memories. *Chem Rev* (2000) 100(5):1755–76. doi:10.1021/cr980072x

40. Al-Aribe KM, Knopf GK, Bassi AS Organic photovoltaic cells based on photoactive bacteriorhodopsin proteins. *Proc SPIE* (2013) 8615:86150Q. 86150Q/1–86150Q/9. doi:10.1117/12.2004018

41. Espinoza-Araya C, Starbird R, Prasad ES, Renugopalakrishnan V, Mulchandani A, Bruce BD, et al. A bacteriorhodopsin-based biohybrid solar cell using carbon-based electrolyte and cathode components. *Biochim Biophys Acta (Bba) – Bioenerg* (2023) 1864(4):148985. doi:10.1016/j.bbabio.2023.148985

42. Lin J, Li X-R, Zhao L-Y, Li G-P, Shen H-Y, Li Y-T, et al. Review on bacteriorhodopsin-based self-powered bio-photoelectric sensors. *Mater Sci Semiconductor Process* (2023) 162:107501. doi:10.1016/j.mssp.2023.107501

43. Chen Z, Birge RR Protein-based artificial retinas. *Trends Biotech* (1993) 11(7):292–300. doi:10.1016/0167-7799(93)90017-4

44. Tsukamoto T, Inoue K, Kandori H, Sudo Y Thermal and spectroscopic characterization of a proton pumping rhodopsin from an extreme thermophile. *J Bio Chem* (2013) 288:21581–92. doi:10.1074/jbc.M113.479394

45. Tsukamoto T, Demura M, Sudo Y Irreversible trimer to monomer transition of thermophilic rhodopsin upon thermal stimulation. *J Phys Chem B* (2014) 118:12383–94. doi:10.1021/jp507374q

46. Oesterhelt D, Stoeckenius W Rhodopsin-like protein from the purple membrane of Halobacterium halobium. *Nat New Biol* (1971) 233:149–52. doi:10.1038/newbio233149a0

47. Lanyi JK Proton transfers in the bacteriorhodopsin photocycle. *Biochim Biophys Acta – Bioenerg* (2006) 1757(8):1012–8. doi:10.1016/j.bbabio.2005.11.003

48. Niho A, Yoshizawa S, Tsukamoto T, Kurihara M, Tahara S, Nakajima Y, et al. Demonstration of a light-driven SO_4^{2-} transporter and its spectroscopic characteristics. *J Am Chem Soc* (2017) 139:4376–89. doi:10.1021/jacs.6b12139

49. Tsukamoto T, Mizutani K, Hasegawa T, Takahashi M, Honda N, Hashimoto N, et al. X-Ray crystallographic structure of thermophilic rhodopsin: implications for high thermal stability and optogenetic function. *J Bio Chem* (2016) 291(23):12223–32. doi:10.1074/jbc.M116.719815

50. Gordeliy VI, Schlesinger R, Efremov R, Büldt G, Heberle J Crystallization in lipidic cubic phases: a case study with bacteriorhodopsin. *Methods Mol Biol* (2003) 228:305–16. doi:10.1385/1-59259-400-X:305

51. Stec HM, Williams RJ, Jones TS, Hatton RA Ultra-thin transparent Au electrodes for organic photovoltaics fabricated using a mixed mono-molecular nucleation layer. *Adv Funct Mater* (2011) 21:1709–16. doi:10.1002/adfm.201002021

52. Sudo Y, Okazaki A, Ono H, Yagasaki J, Sugo S, Kamiya M, et al. A blue-shifted light-driven proton pump for neural silencing. *J Biol Chem* (2013) 288(28):20624–32. doi:10.1074/jbc.M113.475533

53. Reissig L, Mori K, Treadwell R, Dalgleish S, Awaga K Factors affecting the polarity and magnitude of photoresponse of transient photodetectors. *Phys Chem Chem Phys* (2016) 18(9):6821–30. doi:10.1039/C6CP00093B

54. Orazem ME, Tribollet B *Electrochemical impedance spectroscopy*. Deutschland: Wiley (2011).

55. Lima LF, Vieira AL, Mukai H, Andrade CMG, Fernandes PRG Electric impedance of aqueous KCl and NaCl solutions: salt concentration dependence on components of the equivalent electric circuit. *J Mol Liquids* (2017) 241:530–9. doi:10.1016/j.molliq.2017.06.069

56. Reissig L, Dalgleish S, Awaga K Towards high-bandwidth organic photodetection based on pure active layer polarization. *Scientific Rep* (2018) 8:15415. doi:10.1038/s41598-018-33822-z

57. Shcherbakov VV, Artemkina YM, Akimova IA, Artemkina IM Dielectric characteristics, electrical conductivity and solvation of ions in electrolyte solutions. *Materials* (2021) 14(19):5617. doi:10.3390/ma14195617

58. Birge RR Nature of the primary photochemical events in rhodopsin and bacteriorhodopsin. *Biochim Biophys Acta* (1990) 1060(3):293–327. doi:10.1016/0005-2728(90)90163-X

59. Balashov SP Protonation reactions and their coupling in bacteriorhodopsin. *Biochim Biophys Acta* (2000) 1460:75–94. doi:10.1016/S0005-2728(00)00131-6

60. Kouyama T, Nasuda-Kouyama A Turnover rate of the proton pumping cycle of bacteriorhodopsin – pH and light-intensity. *Dependences Biochem* (1989) 28(14):5963–70. doi:10.1021/bi00440a037

61. Bamberg E, Tittor J, Oesterhelt D Light-driven proton or chloride pumping by halorhodopsin. *Proc Natl Acad Sci USA* (1993) 90(2):639–43. doi:10.1073/pnas.90.2.639

62. Vonhoeren B, Dalgleish S, Hu L, Matsushita MM, Awaga K, Ravoo BJ Photocurrent generation in organic photodetectors with tailor-made active layers fabricated by layer-by-layer deposition. *ACS Appl Mater and Inter* (2015) 7:7049–53. doi:10.1021/am509031u

63. Garty H, Klemperer G, Eisenbach M, Roy S The direction of light-induced pH changes in purple membrane suspensions Influence of pH and temperature. *FEBS Lett* (1977) 81:238–42. doi:10.1016/0014-5793(77)80526-7

64. Fotadar U, Zaveloff P, Terracio L Growth of *Escherichia coli* at elevated temperatures J. *Basic Microbio.* (2005) 45(5):403–4. doi:10.1002/jobm.200410542

65. Cahen D, Pecht I, Sheves M What can we learn from protein-based electron transport junctions? *J Phys Chem Lett* (2021) 12(47):11598–603. doi:10.1021/acs.jpclett.1c02446